Interlaboratory testing of thermal properties at ambient pressure on reference samples and core samples from the COSC-1 scientific drill hole,

Geophysical Journal International

Geophys. J. Int. (2025) **241,** 405–436
Advance Access publication 2025 February 04
GJI Heat Flow and Volcanology

https://doi.org/10.1093/gji/ggaf046

Interlaboratory testing of thermal properties at ambient pressure on reference samples and core samples from the COSC-1 scientific drill hole, central Sweden

R. Löwe,[1,2] J. Renner,[1] C. Pascal,[1] B. Adl-Zarrabi,[3] N. Balling,[4] T. S. Bording,[4,5] M. Long,[6] G. Schwarz[7] and J. Sundberg[3,8]

[1]*Institute of Geology, Mineralogy and Geophysics, Ruhr-Univerität Bochum, D-44801 Bochum, Germany. E-mail: joerg.renner@rub.de*
[2]*Bundesgesellschaft für Endlagerung mbH (BGE), Eschenstraße 55, D-31224 Peine, Germany*
[3]*Architecture and Civil Engineering, Chalmers University of Technology, Chalmersplatsen 4, SE-412 96 Gothenburg, Sweden*
[4]*Department of Geoscience, Aarhus University, Høegh-Guldbergs Gade 2, DK-8000 Aarhus C, Denmark*
[5]*TEMcompany ApS, Vester Søgaardsvej 22, DK-8230 Åbyhøj, Denmark*
[6]*School of Civil Engineering, University College Dublin, Richview Newstead Belfield, Dublin 4, 4, Ireland*
[7]*Geological Survey of Sweden, SGU, Villavågen 18, SE-752 37 Uppsala, Sweden*
[8]*JK Innova AB, Åsgatan 1, SE-58228 Linköping, Sweden*

Accepted 2025 January 31. Received 2025 January 14; in original form 2024 May 10

SUMMARY

We conducted comparative measurements of thermal properties of samples from nine cores of the ICDP COSC-1 borehole and four widely used rock references, using a steady-state and a transient divided-bar device, a transient plane source device, a modified Ångström device, as well as two optical thermal conductivity scanners. In addition, a caloric method provided benchmark values for specific heat capacity. A complementary thin-section analysis of the COSC-1 samples allowed us to calculate specific heat capacity according to Kopp's law and thermal conductivity according to commonly used mixing models. Our results demonstrate agreement between the various test methods within ±10 per cent for about one half of the investigated samples. Furthermore, almost all results for specific heat capacity agree with the predictions of Kopp's law, though the significance of this correspondence is limited owing to large uncertainties in the experimental and theoretical values. The results for thermal conductivity fall within the most extreme theoretical bounds that account for anisotropy but for an amphibolite. Thermal anisotropy seems to contribute significantly to the deviations between results of the different transient methods that, however, cannot be reconciled by the available theoretical relations for apparent thermal conductivity of transversely isotropic materials. The combination of characteristic investigation volume of the individual methods and sample heterogeneity has to be considered responsible for variability of results, too, an issue whose clarification is calling for dedicated numerical modelling in the future, with the prospect to characterize thermal heterogeneity from observed differences.

Key words: Europe; Heat flow.

1 INTRODUCTION

An accurate determination of thermal properties of rocks, that is, specific heat capacity, thermal conductivity and thermal diffusivity, is essential for assessing subsurface geothermal states (e.g. Beardsmore & Cull 2001; Andreescu *et al.* 2002; Pasquale *et al.* 2017; Ray *et al.* 2023). Specifically, thermal properties of rocks are instrumental for constraining terrestrial heat flow (e.g. Kohl & Rybach 1996; Fuchs *et al.* 2023; Pascal & Balling 2023) or reconstructing paleoclimate from temperature logs (e.g. Vasseur *et al.* 1983; Rath & Mottaghy 2007) but also for numerous practical applications, such as geothermal energy exploration (e.g. Rosberg & Erlström 2019) and production (e.g. Frey *et al.* 2022; Norden *et al.* 2023) or subsurface nuclear waste storage (e.g. Sundberg & Hellström 2009), and for unconventional analyses of stress transients (e.g. Schmitt *et al.* 2006). The former is the objective of the scientific drilling project 'Collisional Orogeny in the Scandinavian Caledonides' (COSC), supported by ICDP and the Swedish Research Council, aiming at constraining the vertical variation of heat flow

Table 1. Studies comparing techniques for determining thermal properties.

Study	Methods[1]	Number of samples	Sample type	λ range (W m^{-1} K^{-1}); quoted deviation (per cent)
Sass *et al.* (1984)	LS, DB	17	Volcanic and granitic rocks, sediments, metamorphites	1.4–5.0; ±10 per cent
Galson *et al.* (1987)	LS, DB	14	Isotropic rock, polyethylene	0.6–5.4; ±10 per cent
Pribnow & Sass (1995)	LS, DB	81	Amphibolites, gneisses	2.3–4.4; ±10 per cent
Popov *et al.* (1999)	LS, DB, TCS	80	Amphibolites, gneisses	2.0–4.6; ±4 per cent
Pasquale *et al.* (2015)	LS, TDB	–	Fine grained rocks, borosilicate	1.0–4.7; ±2.6 per cent
Bording *et al.* (2016)	LS, DB, TDB	12	Rocks, ceramic	1.6–3.7; 4.6 per cent (TDB–LS), 2.9 per cent (TDB–DB)
Sundberg *et al.* (2003)	TPS, DB	17	Diorites, granites	2.3–3.8; 3 per cent
Kalskin Ramstad *et al.* (2008)	LS, DB, MM	36	Rocks	2.0–4.7; –

1: LS: line source method; DB: divided bar method; TCS: optical scanning; TDB: transient divided-bar method; TPS: transient plane source method; MM: Middleton's (1993) transient method modified at the Geological Survey of Norway

to advance the knowledge of the thermal regime of Palaeozoic orogenic belts and thereby of ancient shield areas and heat-producing plutons, and to improve the understanding of climate change at high latitudes. Reaching these objectives requires converting the temperature logs measured in the borehole at various stages of the project to heat flow data with the help of constraints on thermal properties of the penetrated rocks.

During the past decades, a wealth of approaches were developed to determine thermal properties. Laboratory techniques comprise a range of set-ups and methods, such as the divided bar (e.g. Pasquale *et al.* 2015; Bording *et al.* 2016), the needle probe (e.g. Waite *et al.* 2007), the line-source device (Lubimova *et al.* 1961), the optical thermal conductivity scanner (Popov *et al.* 1985, 1999) and the transient Middleton (Middleton 1993; Kalskin Ramstad *et al.* 2008) and the modified Ångström methods (Andolfsson 2019). The technical development led to a growing number of values of thermal properties for rock-forming minerals (e.g. Birch & Clark 1940; Ratcliffe 1959; Sass 1965; Horai & Simmons 1969; Clauser & Huenges 1995) permitting to estimate bulk thermal properties of rocks employing theoretically motivated averaging schemes, such as Voigt-Reuss averages, with weighting according to quantitative compositional information (e.g. Beck 1988). Other approaches, beyond the scope of this paper, estimate thermal properties by means of emitting and recording thermal signals *in-situ* (e.g. Bullard & Day 1961; Silliman & Neuzil 1990; Pribnow & Sass 1995), using indirect knowledge on mineral phases and *in-situ* porosity (e.g. Brigaud *et al.* 1992; Pascal 2015), or through empirical relationships with lithological and geophysical logs (e.g. Brigaud *et al.* 1990; Fuchs & Förster 2014; Fuchs *et al.* 2015; Meshalkin *et al.* 2020).

The reliability and accuracy of commonly used devices for determination of thermal properties (Table 1) were indirectly assessed by tests on reference materials (e.g. Galson *et al.* 1987; McGuinness *et al.* 2014; Bording *et al.* 2016) and/or directly by using the same sample in several devices (e.g. Popov *et al.* 1999; Sundberg *et al.* 2003). Sass *et al.* (1984), Galson *et al.* (1987), Liebel *et al.* (2011), Pasquale *et al.* (2015) and Bording *et al.* (2016) compared results from newly developed apparatus with those obtained from classical divided bar and line-source devices. These studies quote an average agreement of thermal conductivity values within 3 (Pasquale *et al.* 2015) to 10 per cent (Sass *et al.* 1984) when two or three methods were applied on the same sample in the same laboratory (Table 1). Deviations seem in part systematic, possibly related to loading state and resultant microfracture closing (Galson *et al.* 1987) and/or the degree of anisotropy of the investigated rock samples (Pribnow & Sass 1995; Popov *et al.* 1999; Liebel *et al.* 2011). Popov *et al.* (1999) found for the line-source method that device design and penetration depth of the thermal perturbation affect the reproducibility of results. Sundberg *et al.* (2003) and Liebel *et al.* (2011) extended the comparative studies towards specific heat capacity. Neither reproducibility nor accuracy was reported, hindering the interpretation of deviations between the results from different laboratories.

Our study had the convoluted objectives of providing thermal properties for the specific modelling task at hand in the COSC-1 project and assessing the reliability of the determination of these properties. We consider these objectives exemplary for the situation faced in scientific-drilling projects aiming at constraining the thermal structure of the continental crust. The analysis of thermal logs requires thermal conductivity data. Since *in-situ* measurements of thermal conductivity in deep boreholes continue to be technically challenging, laboratory data remain indispensable. Often, the choice of a measurement method is probably the result of the constellation of project participants rather than of a considerate decision in the light of sample specifics etc. To us, progress in understanding the differences pertaining to the various practiced methods demands more extensive comparison tests than the ones published up to now, in terms of considered methods and the involvement of independent laboratories. To this end, we pursued an interlaboratory testing, focused on crystalline rocks, involving five institutions having six different approaches at their disposal. In addition to samples retrieved from the ∼2.5 km deep ICDP COSC-1 borehole (Lorenz *et al.* 2015), which thanks to the exceptional core retrieval represent all major lithologies penetrated by the well, consisting mainly of gneisses and amphibolites, we investigated a set of reference materials to expand sample diversity.

2 DETERMINATION OF THERMAL PROPERTIES

We employed six different set-ups for determining thermal properties of rocks (Table 2), Dewar flask, steady-state (DB) and transient divided bar (TDB), transient plane source (TPS, HotDisk®), optical scanner (TCS) and modified Ångström (Ång). In the following, we briefly review first the principles of the employed methods, for which the theoretical background is described, for example, in Carslaw & Jaeger (1959) and Beardsmore & Cull (2001). Subsequently, we present theories for calculation of effective thermal properties, dwell on material properties that may affect them, and explain our sample selection.

2.1 Principles of applied measurements

The conductive response of rocks to a thermal perturbation is governed by one scalar property, specific heat capacity per mass, c (J kg^{-1} K^{-1}) or per volume, $\breve{c} = \rho\, c$ (J m^{-3} K^{-1}), with density ρ serving as the conversion factor, and two tensorial properties, thermal conductivity, $\boldsymbol{\lambda}$ (W m^{-1} K^{-1}), and thermal diffusivity, $\boldsymbol{\alpha}$ (m^2 s^{-1}), representing the parameters of a caloric equation of state (A1), a transport law, that is, Fourier's law (A2) and a diffusion

Table 2. Specifics of the measurements (see also Fig. 1). The quoted stresses represent uniaxial stresses applied normal to interfaces in the assemblies to reduce their thermal resistance. The terms 'axial' and 'radial' refer to the directions relative to the cylindrical borehole cores, from which samples were prepared. Owing to the mostly moderate dips (Table 4), 'axial' and 'radial' correspond approximately to perpendicular (⊥) and parallel (∥) to foliation. λ: thermal conductivity, α: thermal diffusivity, c_p, $\tilde{c}_p$ isobaric specific heat capacity (A1)

Method	Thermal gradient[1]		Property		Thermal perturbation		Stress	Research organization
	direction	Δl (mm)	measured	derived	volume	range in T (°C)	(MPa)	
Divided bar (DB)	axial	$\gtrsim 20$	λ_{axial}	/	entire sample, here tens of cm^3	25...40	0.25	University College Dublin (UCD)
Transient divided bar (TDB)	axial	$\gtrsim 20$	λ_{axial}, $\tilde{c}_p$	α_{axial}	entire sample, here tens of cm^3	20... 30	0.5	Aarhus University (AU)
Dewar	/	/	c_p	/	entire sample, here tens of cm^3	30... 60	/	Ruhr-Universität Bochum (RUB)
Modified Ångström (Ång.)	axial	5	α_{axial}	λ_{axial} [2]	slab of tens of mm^3	30... 60	0.14	(RUB)
TC scanner (TCS)	λ: axial; α: radial	/[3]	λ_{axial}, α_{radial}	$\tilde{c}_p$ [4]	profile of mm^3-sized rock volumes	20... 30	/	(RUB)
TC scanner (TCS)	radial$_1$ ⊥ radial$_2$	/[3]	$\tilde{\lambda}_{radial}$ [5]	/	profile of mm^3-sized rock volumes	20... 30	/	Geological Survey of Sweden (SGU)
Transient plane source (TPS)	/[6]	/	λ, α [6]	c_p [4]	half-ellipsoid of up to tenths of cm^3	22... 28	$\leq$0.01	Chalmers University (CU)

1: configuration of points of temperature measurements, relative to sample geometry, with a distance of Δl
2: with $\tilde{c}_p$ from Dewar
3: contact-less temperature measurement for points on the sample surface at different times
4: assuming isotropy
5: see Table A1
6: no directionality because temperature is measured at a single point

equation for temperature T (A4), respectively (e.g. Beck 1988, also Appendix A). The latter results from combining the former two with energy (heat) conservation. The methods for determining thermal properties can be subdivided into two categories, steady-state methods directly exploiting the caloric equation of state and/or Fourier's law, as the 'definitions' for specific heat capacity and thermal conductivity, respectively, and transient methods relying on the diffusion equation with thermal diffusivity as the central parameter scaling rates of local temperature changes and the momentary curvature of spatial temperature distributions.

The results of the various methods employed here (their details given in Appendix B) differ in their significance. The two methods, Dewar-flask calorimetry for the determination of specific heat capacity and steady-state divided bar method for the determination of thermal conductivity, yield results for bulk thermal properties of the tested samples of benchmark character, unbiased by assumptions on isotropy. In contrast, the analyses of temperature records from transient methods rest on an evaluation of the diffusion equation for isotropic media and thus yield equivalent or apparent (e.g. Grubbe *et al.* 1983) properties of a hypothetical isotropic medium that would show the same response to the imposed thermal perturbations as the real material. Whether a transient method constrains two of the three parameters for transport, storage and diffusion depends on the type of temperature perturbation applied. Here, all employed transient methods do but the modified Ångström method, which on its own only constrains thermal diffusivity (Table 2). For anisotropic samples, the calculation of specific heat capacity from individual tensorial conductivity and diffusivity components is inappropriate unless compatible tensorial components are available, which is not the case for the optical scanners that measure temperature transients in two orthogonal directions for the determination of conductivity and diffusivity.

In addition to the fundamental differences originating from the underlying strategies for evaluating temperature records, the various methods differ in technical details regarding, for example, temperature measurements by contact or non-contact methods. Here, only the thermal scanners rely on non-contact temperature measurements. Subtle differences may also arise owing to variations in thermal resistances between the employed heat sources and the sample. To improve heat transfer across assembly interfaces, assemblies are subjected to stresses, a procedure possibly affecting the state of (micro-)fractures in the samples and thereby bulk thermal properties. Besides differences in stress state, differences in further state variables of samples, for example, mean temperature or saturation, come along with the different methods. Finally, the various set-ups differ in the investigated sample volume as a consequence of size and geometry of the heat source and the duration of the thermal perturbation, leading to differences between the results for heterogeneous and anisotropic samples.

2.2 Calculation of effective thermal properties from petrological characterization of sample materials

Specific heat capacity is a volume property and each component of a polyphase aggregate contributes with its heat capacity according to its mass or volume fraction. Thus, the bulk or effective specific heat capacity of a polyphase aggregate results as

$$c_{\text{eff}} = \sum_i \chi_i c_{p,i} \quad \text{and} \quad \tilde{c}_{\text{eff}} = \sum_i \phi_i \tilde{c}_{p,i} \quad , \tag{1}$$

relations known as Kopp's law, where $c_{p,i}$ and $\tilde{c}_{p,i}$ denote the specific heat capacity and thermal capacity of component i, and χ_i and ϕ_i its mass and volume fractions, respectively (e.g. Clauser 2011a).

Thermal conductivity is a structure-dependent transport property, for which only bounds can be constrained from known composition. The mineral properties along with orientation distribution in a rock determine the degree of anisotropy. The widest bounds for the effective thermal conductivity of a multiphase aggregate are the Voigt and Reuss bounds that respectively coincide with the arithmetic mean (upper bound)

$$\lambda_{\text{Voigt}} = \sum_i \phi_i \lambda_i \tag{2}$$

and the harmonic mean (lower bound)

$$\frac{1}{\lambda_{\text{Reuss}}} = \sum_i \frac{\phi_i}{\lambda_i} \quad , \tag{3}$$

where λ_i denotes the thermal conductivity of component i and ϕ_i its volume fraction (e.g. Jessop 1990; Beardsmore & Cull 2001; Clauser 2011a). Eqs (2) and (3) correspond to heat flow parallel and perpendicular to layered structures of isotropic materials, respectively (Cernuschi *et al.* 2004). When different isotropic components or a single anisotropic component are randomly distributed, macroscopic isotropy results. Then, the effective thermal conductivity obeys the rigorous upper and lower Hashin−Shtrikman bounds (e.g. Clauser 2011b) that are tighter than the Voigt–Reuss pair. These bounds have to be employed in (2) and (3) for the calculations of the effective thermal conductivity of a medium comprising

isotropic layers. Often the geometric mean

$$\lambda_{\text{geom}} = \prod_i \lambda_i^{\phi_i} \tag{4}$$

is evoked that presumably describes randomly distributed and orientated components in a mixture (Beardsmore & Cull 2001) but has no rigorous geometrical interpretation (Jessop 1990) and is empirically rather than physically based (Beck 1988). The geometric-mean mixing model gained its popularity from its relatively good match with observations (Jessop 1990). For example, Pasquale *et al.* (2017) state a difference of 5 to 10 per cent between values measured and estimated according to the geometric mean.

The growing number of values for thermal properties of rock-forming minerals reported in the literature (e.g. Birch & Clark 1940; Ratcliffe 1959; Sass 1965; Horai & Simmons 1969; Waples & Waples 2004) permits to estimate thermal rock properties employing the presented averaging schemes. In fact, the compilation of literature data by Waples & Waples (2004) suggests that calculations of specific heat capacity based on Kopp's law (1) may be superior to measurements on rock samples.

Generic concepts for constraints on effective thermal diffusivity of heterogeneous media are not known. In particular, the simple calculation using the above described effective specific heat capacity and (bounds on) thermal conductivity in (A4) lacks any justification, but the effective behaviour will depend on the specifics of the thermal perturbation (see Carson 2022).

2.3 Material properties and state variables affecting thermal properties

Composition is of prime importance for effective thermal properties of aggregates, as is obvious from the theoretical relations (1, 2 and 3). Yet, for the transport properties, thermal conductivity and diffusivity, the (micro-)structure is equally relevant. Bulk anisotropy may result from layering of components and/or preferred orientations of anisotropic components and of non-equant voids. Thermal anisotropy is documented for some of the common rock-forming minerals. The thermal conductivity of quartz differs by almost a factor of two between the least and best thermally conductive crystal axes, while for sheet silicates the anisotropy factor is about five to six (Table F1).

For minerals, specific heat capacity increases (e.g. Waples & Waples 2004) while thermal conductivity decreases (e.g. Clauser 2011a) with increasing temperature. The relative changes in either case range between 0.1 and 0.3 per cent K^{-1}, and combine to a relative decrease in thermal diffusivity with temperature of up to 0.6 per cent K^{-1}. The review of Schön (2015) suggests an increase in thermal conductivity λ of minerals and rocks with pressure of $\lesssim 0.015$ per cent MPa^{-1}; likewise, Waples & Waples (2004) conclude on an increase in isobaric specific heat capacity c_p with pressure of $\lesssim 0.015$ per cent MPa^{-1} from their literature study. As a consequence of these similar increases, their effects cancel leading to a negligible effect of pressure on thermal diffusivity α (see also Norden *et al.* 2020).

The presence of voids in rocks, that is, pores and fractures, may significantly affect their thermal properties (e.g. Walsh & Decker 1966). The specific heat capacity and thermal conductivity of air are so low that the difference between calculations for evacuated and air-filled voids is negligible. For example, at ambient conditions, the specific heat capacity and thermal conductivity of air are more than three and about two orders of magnitude smaller than that of minerals, respectively. While the effect of air-filled voids on specific heat capacity simply scales with their volume fraction, that is, porosity, and thus may at most lead to a reduction of tens of per cent, the reduction in thermal conductivity depends on the geometrical features of the voids and may be significant even for low porosities (e.g. Sevostianov 2006; Nguyen *et al.* 2017; Li *et al.* 2021). In contrast, the specific heat capacity of water is about twice as large per unit volume as that of common rock-forming minerals, and thus the effective specific heat capacity of saturated porous rocks may actually exceed that of dense rocks. At ambient conditions, the thermal conductivity of water is about 0.6 $W\,m^{-1}\,K^{-1}$, corresponding to only a tenth to a third of that of common rock-forming minerals. Thus, effective thermal conductivity for a specific rock increases with water saturation but that of a suite of rocks generally decreases with increasing porosity, irrespective of whether the pore space is empty, air-filled or water-saturated.

The role of voids in transient thermal processes is unfortunately not well investigated (e.g. Carson 2022), and the intuition developed from the classical approaches to constrain effective specific heat capacity and thermal conductivity for steady state (presented in the previous section), effect is not transferable. In fact, the thermal diffusivity of air is more than one and three orders of magnitude larger than that of minerals and water, respectively. It increases with temperature but decreases with pressure. Thus, the effect of air-filled voids on transient processes is expected to be strikingly different than that on steady-state processes. Judging from the thermal diffusivity, air-filled voids are 'responsive' to transient thermal perturbations. The thermal diffusivity of water, in contrast, is about an order of magnitude smaller than that of minerals. It increases with temperature and modestly with pressure. Water-filled voids may thus act as heat sinks retarding heat diffusion.

In rocks, the intrinsic pressure effect on thermal properties of minerals may be overlapped by that of stress on the geometrical aspects of voids. A reduction in porosity due to pressure or stress leads to a modest increase in specific heat capacity but possibly to a significant increase in thermal conductivity depending on the specific microstructure (e.g. Walsh & Decker 1966). Changes in thermal diffusivity of rocks containing compliant voids with stress are hardly investigated, be it experimentally or theoretically (but see McDonald *et al.* 2001; El Yagoubi *et al.* 2019). Seipold & Huenges (1998) investigated the effect of pressure and temperature on thermal properties of gneisses, and reported a reduction in anisotropy with increasing pressure, which suggests that the role of microfractures for bulk anisotropy may dominate over that of mineral-layering complicating predictions on principal axes of the thermal transport properties.

2.4 Sample selection, preparation and workflow

Our study's convoluted objectives, of establishing a reliable data base for the COSC-1 borehole and performing an interlaboratory comparison, necessitate to address absolute accuracy, which is problematic if restricting to the COSC-1 drill cores with unknown properties alone. Therefore, we included four materials, namely Carrara marble, Westerly granite and commercial pyrophyllite and Al_2O_3 ceramic (Table 3), addressed as reference materials in the following. These have previously been used in laboratory studies including determination of their thermal properties (Birch & Clark 1940; Carte 1955; Robie *et al.* 1976; Heuze 1983; Chen & Decker 1992; Robertson & Hemingway 1995; Vretenár *et al.* 2007; Kubičár *et al.* 2008, 2015), according to which they represent almost the full range of

Table 3. Thermal conductivity λ and isobaric specific heat capacity c_p of reference materials.

Reference material	λ (W m^{-1} K^{-1})	c_p (J kg^{-1} K^{-1})	Reference
Carrara marble	2.3 (at 273.5 K)	851 (at 273.5 K)	Vretenár *et al.* (2007)
Westerly granite (orange)	2.4 (at 273.5 K)		Birch & Clark (1940)
		818 (at 338.7 K)	Robertson & Hemingway (1995)
Pyrophyllite (unfired)[1]	∥: 5.4 (at 356 K) ⊥: 3.0 (at 356 K)		Chen & Decker (1992)
		815	Robie *et al.* (1976)
Al_2O_3 ceramic (Degussit AL23)	34.9 (at 373 K)	900 (at 293 K)	as specified by producer Kyocera

1: parallel (∥) and perpendicular (⊥) to foliation

thermal conductivity relevant for rocks and minerals, for example, λ from 2.3 to 34 W m^{-1} K^{-1}. The two monomineralic aggregates, Carrara marble and Al_2O_3 ceramic, allow us to use mineral data for the calculation of their effective properties without the additional complication of uncertain composition. The two rocks, Carrara marble and Westerly granite, are also considered to constitute approximately isotropic aggregates (e.g. Schubnel *et al.* 2006), while the pyrophyllite samples are prototypically anisotropic (Chen & Decker 1992).

Before the selection of COSC-1 samples, cores of about 20 cm individual length and a combined length of about 21 m, sampled every ∼25 m over the entire depth range of the drill hole, were scanned with an optical thermal conductivity scanner (Block *et al.* 2024). Cores have a diameter of 61 mm down to 1616 m and 47 mm below this depth, the latter size slightly falling below the recommended minimal diameter of 60 mm for the used optical scanner. We used an aluminum passe-partout to ensure proper alignment of the cores relative to the heat source and the temperature measurement spots.

The scans provided continuous profiles of λ and α along the surfaces of the cylindrical core pieces (Fig. 1). Based on the scan results, nine core pieces (Table 4) were selected for the interlaboratory testing since they (i) exhibit relatively constant thermal properties over the 20 cm long scan lines, (ii) represent the major lithologies penetrated by COSC-1 and (iii) evenly cover the depth range of the well.

For our interlaboratory study, we refrained from aiming at determining thermal properties on the same samples because of the different sample-size requirements of each method (Table C1) and the logistical challenges of a round robin. Instead, from each of the selected core pieces of the COSC-1 well bore, samples were prepared for each of the five participating laboratories, according to their specifications (Table C1). Likewise, each laboratory received a set of samples from the reference materials. The differences in size requirements made it necessary to work with similar but not identical samples adding sample-to-sample variation as a potential source for differences between results of the various methods. Including the reference materials in our study intended to evaluate our results for the COSC-1 cores in the light of that for materials that are nominally simple or exhibit one specific feature and are at the same time representative for crystalline, close to dense rocks. A purely methodological study should rely on a round robin of well-defined references, probably not found among rocks.

Cylindrical samples of the required dimensions were prepared by water-cooled diamond drilling, sawing and grinding at RUB (institution acronym's are introduced in Table 2). Density, for example, needed for conversion between specific heat capacity and thermal capacity, was determined from weighing and volume determination (geometrical at UCD; using Archimedes' principle at RUB). These two laboratories also determined connected porosity of samples from mass differences between water saturated and dry samples.

Each laboratory performed thermal tests on its set of samples (Fig. 1), in the majority of cases 'as delivered', because not all the measuring procedures included in this study are suitable for studying water-saturated rock samples, the likely *in-situ* state. The following results section focuses on the results of these measurements. However, two of the involved laboratories additionally performed experiments on 'dry' and 'water-saturated' samples to quantitatively test the often formulated expectation that the effect of water-saturation on thermal conductivity is subordinate for low-porosity materials, as the COSC-1 core samples (e.g. Jessop 1990), and to assess the relevance of possible differences in the water content of samples due to shipping and differences in the laboratory conditions of the involved institutions. In all cases, the temperature perturbations took place under constant pressure, and thus we use the common notation for isobaric specific heat capacity, c_p.

Residual material from the samples prepared for modified Ångström measurements at RUB was used for the preparation of thin sections (∼20 mm wide, ∼40 mm long, 0.03 mm thick) with their long side orientated parallel to the core axis for optical-light microscopy at RUB. Mineral phases were identified and their average volume fractions and standard deviations estimated from point counting (Appendix E) to exploit the theoretical relations for effective thermal properties (1, 2, 3). We refrained from amending the petrographic analysis by XRD analyses providing additional constraints on mineral fractions, because compositional uncertainty does not dominate the uncertainty of calculated effective properties.

3 RESULTS

3.1 Basic physical properties

Tested samples cover a range in density from 2600 to 4000 kg m^{-3} (Fig. D1). The density values determined at RUB for COSC-1 cores and samples prepared from them agree within uncertainty but for the pegmatite (C309S3). Though density-composition relations are by no means unique, this consistency supports the notion of compositional homogeneity on the core scale, a pre-requisite for our sampling strategy. Furthermore, the correlation of results by RUB and UCD (Fig. D1) suggests a systematic shift between the two data sets (the UCD density values about 10 to 20 kg m^{-3} higher than the RUB density values) rather than random sample-to-sample

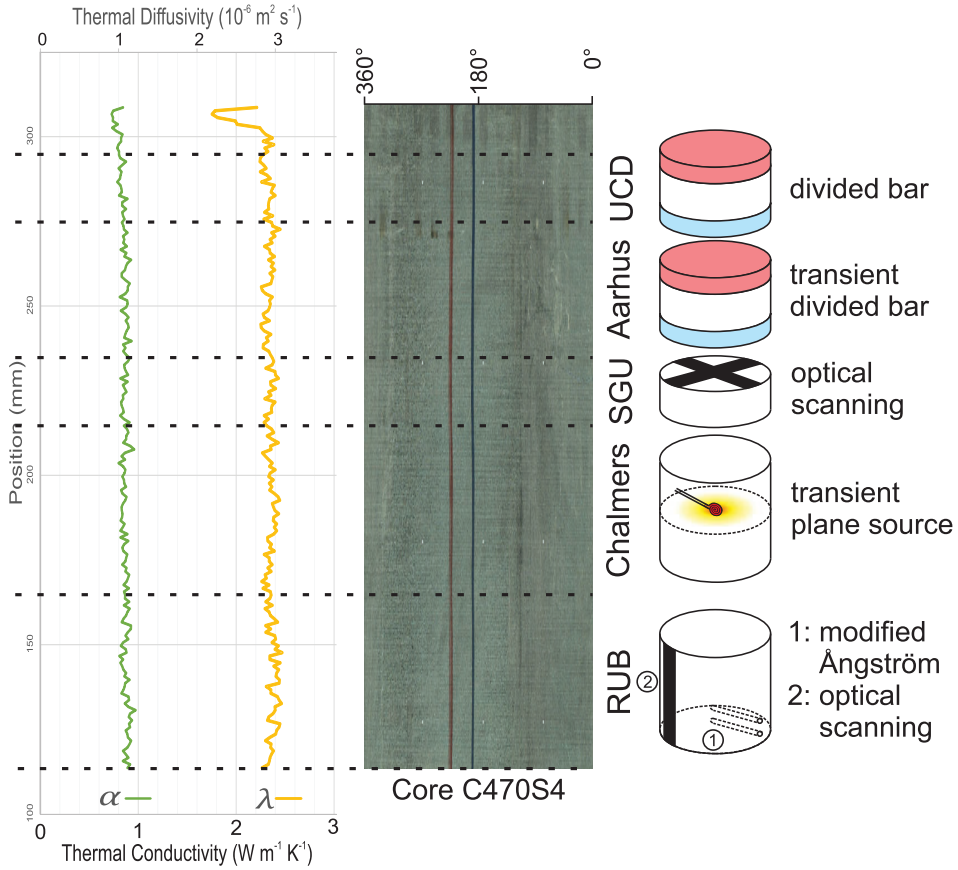

Figure 1. The thermal conductivity scanning profile for sample C470S4 (1447.8 m, amphibolite) showing λ (yellow, line on the right, bottom x-axis) and α (green, line on the left, top x-axis) against position along the core surface (plot on the left). The optical surface scan of the core (centre) indicates a fairly homogeneous sample. Dashed lines indicate the respective sample pieces sent to each partner of the interlaboratory test. Individual testing configurations are depicted in the sketches on the right. Scanlines of the optical scanners are indicated by black lines. Red and blue discs indicate the heat sources and sinks for the transient and steady-state divided bar devices.

Table 4. COSC-1 core pieces selected for the inter-laboratory test.

IGSN[1] ICDP5054...	C#S#[2]	Depth[3] (m)	Diameter (mm)	Lithology	Dip[4] (°)
EXP0601	C7Z1	116.0	60.9	Coarse grained paragneiss	~45
EX71601	C150S2	525.0	61.0	Amphibolitic gneiss	massive
EXM1601	C272S1	872.5	~ 61	Calc-silicate gneiss	~0
EXJ6601	C309S3	976.4	60.6	Pegmatite	~20
EX22601	C404S2	1251.1	60.8	Calc-silicate gneiss	~40
EX92601	C470S4	1447.8	61.0	Amphibolite	~20
EX23601	C635S5	2128.3	47.6	Quartz-rich granitoid gneiss	~30
EX73601	C652S1	2225.9	47.5	Mylonite	~25
EXE6601	C686S1	2430.4	47.4	Paragneiss	~10

1: International GeoSample Number (drill hole ICDP 5054-1-A); access at, for example, https://dataservices.gfz-potsdam.de/igsn/icdp/index.php?igsn=ICDP5054EXP0601
2: Core number and section number
3: Driller's depth
4: Dip of foliation relative to the core cylinder top.

variability. Porosities of COSC-1 samples do not exceed 1 per cent. Yet, not all porosity values of samples originating from the same core determined in the two laboratories agree within uncertainties, possibly reflecting variability in microfracture characteristics. For the reference materials, density values determined in the two laboratories at UCD and RUB agree within uncertainty except for Carrara marble, possibly indicating natural variability.

3.2 Effective property calculation for COSC-1 samples

The majority of the selected COSC-1 rocks exhibit a macroscopically visible foliation that we characterize by dip angles determined on the cores, as the angles included by the core axes and the normal vector to the foliation planes. The thin-section analysis revealed that the foliation is related to sorting and banding of mineral phases (Fig. 2). Only three minerals dominate the compo-

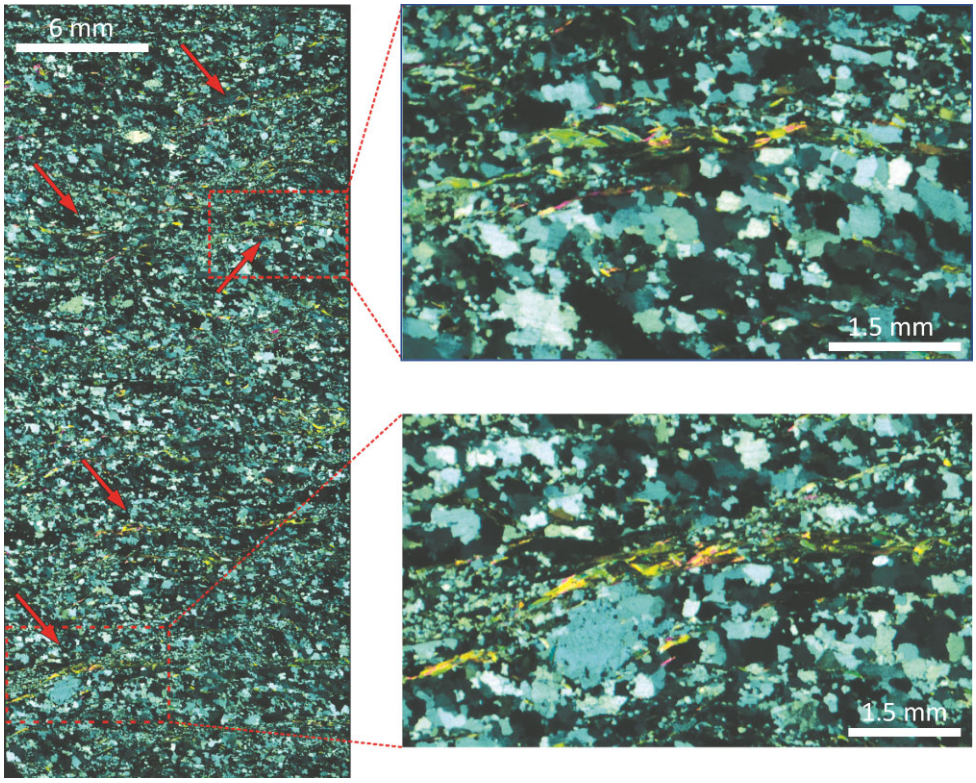

Figure 2. Microphotographs of the thin section of sample C635S5 (2128.3 m, quartz-rich granitoid gneiss, dip ∼ 33°) in cross-polarized light. On the left, arrows indicate continuous mica layers following the foliation. On the right, two of the mica bands within the quartz matrix are magnified.

sitions of the investigated COSC cores, that is, quartz, microcline and amphibole, with volume fractions of $\gtrsim$ 40 vol per cent. Quartz is the most abundant mineral phase, except in the amphibolitic gneiss and the amphibolite sample (Table E1). Carbonate, biotite and plagioclase occur with 10 to $\lesssim$ 20 vol per cent, and chlorite and garnet are only accessory minerals in three of the nine cores. In the following, we use the combined volume fractions of quartz and mica to classify samples as having a low ($\leq$44 vol per cent) or a high (>44 vol per cent) content of thermally anisotropic minerals.

Based on the determined volume fractions of minerals (Table E1) and relevant published $\tilde{c}$ and λ values (Table F1), effective specific heat capacity and thermal conductivity were calculated (Table 5), the former according to Kopp's law (1) and the latter according to Voigt and Reuss averaging schemes as well as the geometric mean, (2) to (4). The observed low porosity values do not significantly affect the specific-heat capacity calculations and were, therefore, neglected. We disregarded potentially systematically orientated microfractures in the conductivity calculations, owing to the absence of constraints on them. For the Voigt and Reuss limits, we considered two scenarios, isotropic layers and anisotropic layers, the latter accounting for the anisotropy of thermal conductivity on the level of the individual mineral phases. We assumed that mineral orientation is systematic in anisotropic layers, such that minimum and maximum λ values for anisotropic minerals served, respectively, as input for the Reuss and Voigt models producing the most extreme bounds. For the geometric mean, we used the Voigt–Reuss–Hill averages of conductivity reported for the components.

Uncertainties of the effective heat capacities were calculated by Gaussian error propagation accounting for the uncertainty in mineral volume fractions and in the reported thermal properties. We used the standard deviation of mineral counts on four lines per thin section as a measure of the uncertainty for the determined volume fractions. Since solid solution series (i.e. carbonates, plagioclase and garnets) are only present in modest volume fractions (Table E1), the uncertainty about the exact compositions and their thermal properties does not significantly affect the calculation of effective properties. Because uncertainties in thermal capacity and thermal conductivities for the relevant minerals are not consistently reported in the literature, we uniformly assumed an uncertainty of 10 per cent. We refrained from reporting uncertainties for the Voigt and Reuss conductivity bounds because they already reflect an uncertainty that in the appropriate structure model, and their spreads are much wider than uncertainties due to that of input parameters.

The calculated effective specific heat capacity values nominally range from 690 to 810 J kg^{-1} K^{-1} but overlap for all samples within their uncertainties (Table 5). The effective thermal conductivities exhibit a variation by a factor of 2 in the suite of samples for a given averaging scheme. The upper (Voigt) bound for anisotropic layers is two to four times larger than the corresponding lower bound. The conductivity bounds for the isotropic layers provide ranges in values that are only slightly wider than those given by the geometric means and their uncertainties.

3.3 Effect of saturation state on thermal conductivity

Samples were investigated 'as delivered', 'dry' and 'saturated' with the two divided-bar methods, steady-state and transient. Their results deviate regarding the effect of water saturation on effective thermal properties of the reference samples and the COSC-1 samples. Drying samples reduced thermal conductivity measured with

Table 5. Effective thermal capacities $\tilde{c}$ and specific heat capacities $c_p = \tilde{c}/\rho$ (1), and thermal conductivities λ_V (2), λ_R (3) and λ_{geom} (4) calculated from mineral volume fractions of COSC-1 samples (Table E1) using literature values for the mineral properties (Table F1). The subscripts 'il' and 'ail' indicate calculations for isotropic and anisotropic layers (see text for details). Sample densities are compiled in Table C1.

ID[1]	$\tilde{c}$ ($MJ\,m^{-3}\,K^{-1}$)	c_p ($J\,kg^{-1}\,K^{-1}$)	$\lambda_{V,il}$	$\lambda_{V,ail}$	$\lambda_{R,il}$ ($W\,m^{-1}\,K^{-1}$)	$\lambda_{R,ail}$	λ_{geom}
C7Z1	2.09±0.09	768±35	4.8	5.8	3.5	3.2	4.0±0.5
C150S2	2.22±0.10	749±34	3.6	4.3	2.8	1.7	3.0±0.3
C272S1	2.08±0.09	778±35	6.0	7.8	4.4	2.0	5.3±0.7
C309S3	1.89±0.09	724±33	4.2	5.2	2.9	2.5	3.4±0.5
C404S2	2.09±0.09	774±35	4.7	5.8	3.4	2.8	4.0±0.5
C470S4	2.22±0.10	738±33	3.0	3.2	2.6	2.5	2.7±0.3
C635S5	2.01±0.09	752±34	6.6	8.8	5.3	2.5	6.1±0.2
C652S1	2.03±0.09	754±34	6.2	8.4	4.7	1.9	5.6±0.5
C686S1	1.98±0.09	736±33	6.6	8.8	5.3	2.6	6.1±0.6

1: see Table 4 for IGSN

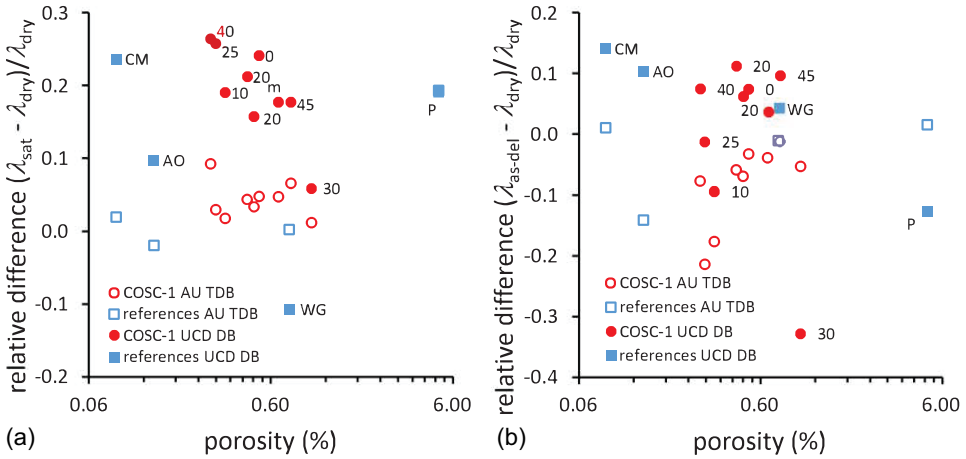

Figure 3. Difference between thermal conductivity of (a) saturated and dry samples, and (b) as delivered and dry samples, determined in divided bar measurements (DB: steady-state; TDB: transient), normalized by the result for dry samples, that is, $(\lambda_{sat} - \lambda_{dry})/\lambda_{dry}$ and $(\lambda_{as-delivered} - \lambda_{dry})/\lambda_{dry}$, for samples from the COSC-1 cores and the selected reference materials (CM: Carrara marble, WG: Westerly granite, P: pyrophyllite, AO: aluminium oxide Al_2O_3) as a function of porosity determined from weight gain due to water saturation. The number labels give the approximate dip values for the COSC-1 samples (Table 4). For presentation purposes, only UCD DB data are labelled, but dip estimates can be associated to the AU TDB data owing to the unique porosity values.

the steady-state method by less than 10 per cent on average and saturation increased it by about 20 per cent on average (Fig. 3) compared to the 'as delivered' state.

The effects of sample saturation were generally less pronounced for the measurements using the transient divided-bar method than for that using the steady-state device. Notably, drying increased thermal conductivity on average by 5 per cent relative to the 'as delivered' state, in qualitative agreement with the increase in thermal diffusivity when replacing water by air. Yet, the thermal conductivity of fully saturated samples tends to exceed their conductivity when dry, on average by about 5 per cent, which is significantly less than the effect of saturation observed with the steady-state method. Although the origin of the difference in the results of the two methods will require further discussion, at face value, the differences in thermal conductivity of 'dry' and 'saturated' samples does not exceed 20 per cent, that is, remains almost within the maximum possible experimental uncertainty of 10 per cent for each measurement. This spread can thus be considered a pessimistic uncertainty of results for samples tested 'as delivered' in different laboratories.

3.4 Thermal properties—reference samples

3.4.1 Specific heat capacity

For the Dewar method, we extended the suite of reference samples by the four standards used for the optical scanner at RUB (Table A2). The values deduced from our measurements cover a range from below 500 to almost 1000 $J\,kg^{-1}\,K^{-1}$ and agree within their uncertainties with those given for the standards (Fig. 4a). The significant deviations of the Dewar results from the literature values for Carrara marble and Al_2O_3 ceramic may suggest material differences. The Dewar results, however, match the mineral data of 754 $J\,kg^{-1}\,K^{-1}$ for corundum, but indeed fall somewhat short of that of 815 $J\,kg^{-1}\,K^{-1}$ for calcite (Waples & Waples 2004).

Specific heat capacity c_p of the reference materials was directly determined using the Dewar method and deduced from the temperature records of three transient methods (Table 2). Density values measured at RUB (Appendix D) were employed in the calculations when necessary. The values gained for the four reference materials from transient methods cover a similar range as the ones from the Dewar method, that is, about 600 to 900 $J\,kg^{-1}\,K^{-1}$, except for the high value, compared to the others, from TPS measurements on

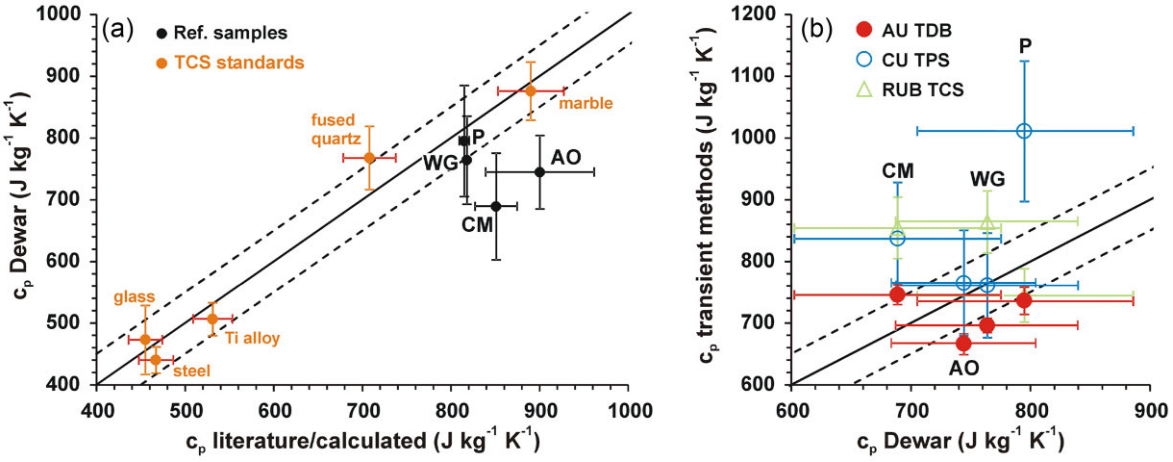

Figure 4. (a) Correlation of specific heat capacity c_p of the reference samples and TCS standards, as measured with the Dewar method, versus their respective literature values (Tables 3 and A2). The c_p values of the TCS standards were calculated using (A8). Horizontal error bars represent error ranges derived from TC scans, that is, 6 per cent. (b) Specific heat capacity c_p of the reference materials determined with transient methods versus specific heat capacities determined with the Dewar method. Solid and dashed lines indicate the '1:1'-line ±10 per cent. CM.: Carrara marble; WG: Westerly granite; P.: Pyrophyllite; AO: Al_2O_3 ceramic.

pyrophyllite (Fig. 4b, Table 3). For Carrara marble, the results of TPS and TCS deviate the most from those found with the Dewar method.

3.4.2 *Thermal conductivity*

Thermal conductivity determined for the reference samples ranges from 2 to above 30 $W\,m^{-1}\,K^{-1}$ reasonable agreeing with the literature values (Fig. 5a). For Carrara marble and Westerly granite, the results of the transient methods are consistent with the steady-state divided bar results within uncertainty, including even the modified Ångström approach, for which conductivity had to be derived from the determined thermal diffusivity employing specific heat capacity determined with the Dewar method. The results of the transient methods for pyrophyllite and the Al_2O_3 ceramic tend to exceed those of the steady-state divided bar method, the nominal conductivity benchmark. Most data for pyrophyllite, however, fall between the principal conductivity values previously reported for directions normal and parallel to foliation (i.e. $\lambda_\perp$ and $\lambda_\parallel$); only the TDB result is above that range by about 1 $W\,m^{-1}\,K^{-1}$. Specifically, the steady-state divided bar method yields a thermal conductivity close to $\lambda_\perp$, as do thermal scanning at RUB and the modified Ångström method, while the three other transient methods give results closer to $\lambda_\parallel$, reflecting the differences in the geometrical specifics of temperature measurements inherent to the methods (Table 2).

While in cases barely, the results of the four methods that succeeded to measure the thermal conductivity of the Al_2O_3 ceramic are, within uncertainty, consistent with the value quoted by the manufacturer. The TPS value exhibits the closest agreement with the latter reference value, all others tend to be too low. The steady-state divided bar method yields a conductivity that is too low by about a factor of five, probably reflecting that the conductivity of the Al_2O_3 ceramic exceeds the measurement range of this device, quoted to be between 1 and 10 $W\,m^{-1}\,K^{-1}$ (Popov *et al.* 2016). Likewise, methodological limits are indicated for the optical scanning devices. The scanning of the cylinder sidewalls conducted at RUB did not provide interpretable temperature profiles, while scans of the flat end faces conducted at SGU provided plausible thermal conductivity results.

Excluding the results for the exceptionally conductive Al_2O_3 ceramic, we note that the highest values were systematically obtained with the transient divided-bar method. The lowest values come from the Ångström method, for Carrara Marble and Westerly Granite, and from the steady-sate divided bar, for pyrophyllite. The two latter methods gave systematically rather low values for all tested reference materials. Nevertheless, thermal conductivities measured on relatively isotropic materials showed moderate dispersion (i.e. standard deviations of 0.18 and 0.16 $W\,m^{-1}\,K^{-1}$ for Carrara Marble and Westerly Granite, respectively), whereas they yielded significant scatter in the case of pyrophyllite (i.e. standard deviation of 1.03 $W\,m^{-1}\,K^{-1}$).

3.4.3 *Thermal diffusivity*

Thermal diffusivity results for the reference materials range from 1.1×10^{-6} to 10.8×10^{-6} $m^2\,s^{-1}$. They exhibit fair agreement among each other and with literature data, except for the anisotropic pyrophyllite sample (Fig. 5b). For the latter, the transient divided bar yielded an exceptionally high value, even in the light of the two α values calculated based on the $\lambda_\parallel$ and $\lambda_\perp$ values reported in the literature. It was not possible to determine α of the Al_2O_3 ceramic with the modified Ångström device or the TCS at RUB. The TDB results tend to exceed those obtained with the other devices.

3.5 Thermal properties—COSC-1 samples

3.5.1 *Specific heat capacity*

Specific heat capacity values gained for the COSC-1 samples by the Dewar method show a spread of 100 $J\,kg^{-1}\,K^{-1}$ almost twice as much as that of values gained from calculations based on Kopp's law (Fig. 6d, Table 5). The two results, however, agree when uncertainties are taken into account.

Specific heat capacity values gained for the COSC-1 samples by the transient methods range between 632 and 848 $J\,kg^{-1}\,K^{-1}$

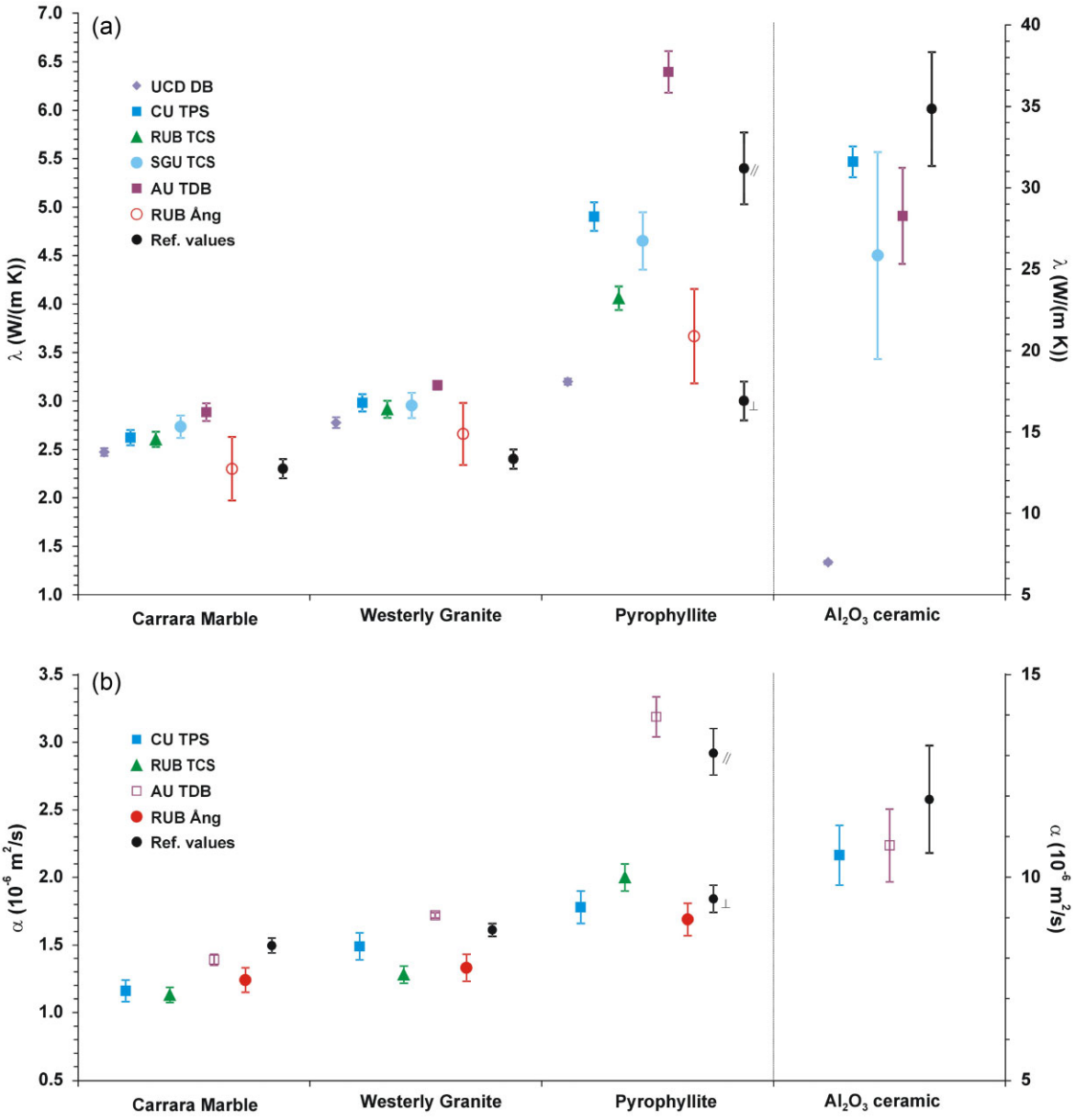

Figure 5. (a) Thermal conductivity and (b) thermal diffusivity for the reference materials investigated at AU, CU, RUB, SGU and UCD employing transient divided bar (TDB), transient plane source (TPS), modified Ångström (Ång) and steady-state divided bar (DB) devices as well as two optical thermal conductivity scanners (TCS). Solid symbols indicate that thermal conductivity λ was measured directly. The right vertical axes refer to Al_2O_3 results. The principal components of the conductivity tensor for heat flow perpendicular and parallel to foliation for pyrophyllite are labelled by ⊥ and ∥, respectively.

(Fig. 6). Values determined with the TDB and the TPS devices tend to be lower than those measured by the Dewar method, whereas, data from the TCS used by RUB scatter unsystematically around the Dewar results. All data from TDB and TPS agree with each other and with the Dewar ones within the corresponding measurement uncertainties. The TDB data exhibit the lowest average deviation from the results of the Dewar method, that is, 50 $J\,kg^{-1}\,K^{-1}$. Contrarily, the largest average deviation between two methods was found for the TDB results and the TC scans, that is, 92 $J\,kg^{-1}\,K^{-1}$.

The standard deviations of the c_p-data from the various methods correlate with the sample's content of anisotropic minerals, though structure should not affect the volumetric property c_p. For the coarse grained paragneiss (C7Z1) with a moderate content of anisotropic minerals, the standard deviation is about three times smaller than for the mylonite sample (C652S1) with a high content of anisotropic minerals.

3.5.2 Thermal conductivity

Thermal conductivity of COSC-1 samples ranges from 1.7 to 5.5 $W\,m^{-1}\,K^{-1}$ (Table 2, Fig. 7a). Absolute differences between results of different measuring approaches range from 0.2 (i.e. the amphibolite sample, C470S4) to 3.1 $W\,m^{-1}\,K^{-1}$ (i.e. the granitoid gneiss sample, C635S5). The TC scanning conducted at SGU and the measurements with the TDB device exhibit the lowest average difference, that is, 0.2 $W\,m^{-1}\,K^{-1}$. Data from the RUB-TCS and from the DB device exhibit the highest average deviation, that is, 0.9 $W\,m^{-1}\,K^{-1}$.

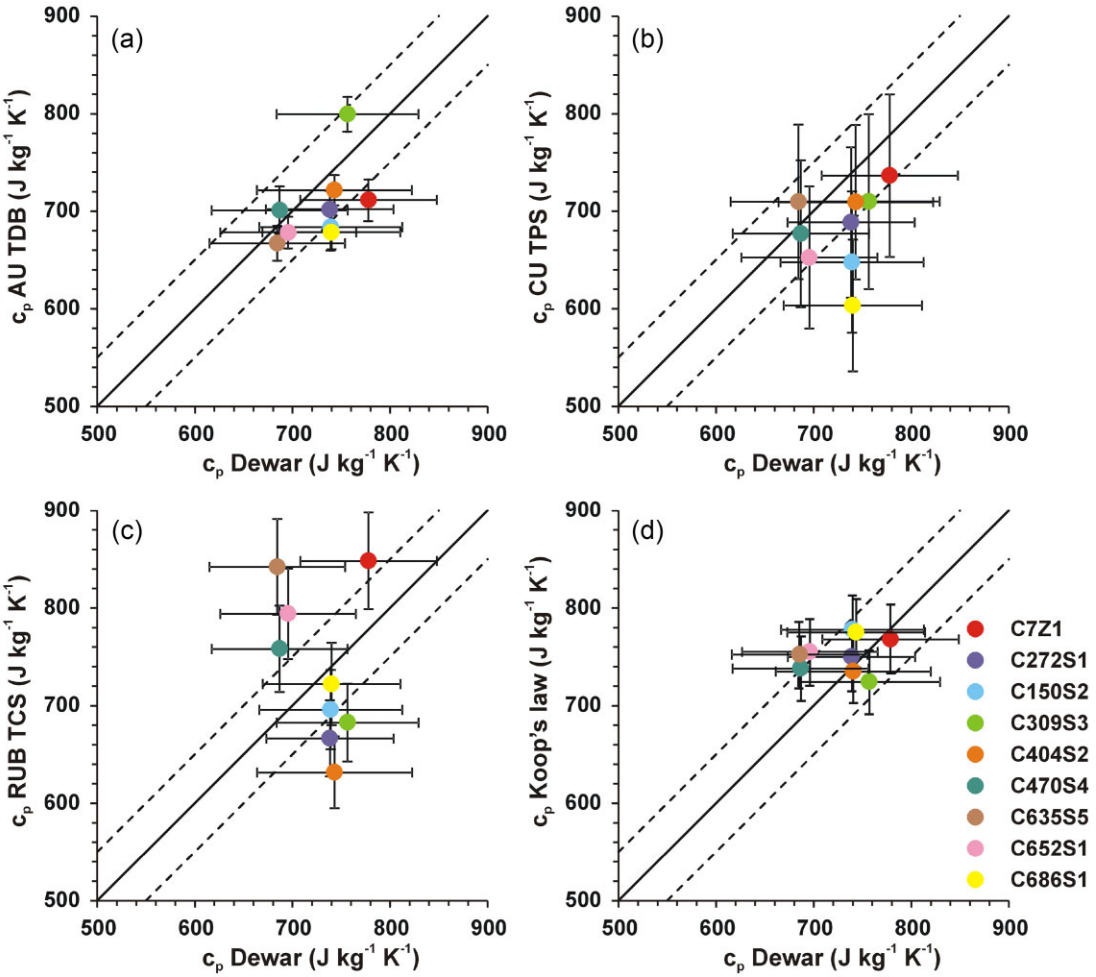

Figure 6. Specific heat capacity c_p for the COSC-1 samples determined with transient methods versus specific heat capacity determined with the steady-state Dewar method: (a) the transient divided bar (TDB), (b) the transient plane sources (TPS) and (c) the optical thermal conductivity scanner (RUB TCS). (d) Comparison of specific heat capacity c_p calculated according to Kopp's law (1) using compositions of the COSC-1 cores given in Table E1 and literature values given in Table F1 and the experimental results of the Dewar method. Dashed lines indicate the '1:1'-line ±10 per cent. The colour coding refers to the different COSC-1 samples, as indicated by the legend in (d) that holds for all plots.

In general, λ-results tend to plot between the Reuss average and the geometric mean. For the amphibolite sample (C470S4), all mixing models provide λ values above the measurement results. The spread of data for a specific sample increases with the content of anisotropic minerals, mimicking the widening of the bounds of the mixing models. Deviations in data between the methods are smallest for samples with a low fraction of anisotropic minerals. For samples with a high content of anisotropic minerals, results of the modified Ångström and the DB device are constantly below the ones of the other methods, and the DB results are generally below the ones of the modified Ångström device (Fig. 7a).

3.5.3 Thermal diffusivity

Obtained thermal diffusivity values range from 0.8×10^{-6} to 2.9×10^{-6} m^2 s^{-1} (Fig. 7b). The absolute difference between all measurements ranges from 0.2×10^{-6} m^2 s^{-1} (calc-silicate gneiss, C404S2) to 1.2×10^{-6} m^2 s^{-1} (granitoid gneiss, C635S5). The highest average deviation over all COSC-1 samples was found between the results from the modified Ångström method and the TPS device, that is, 0.4×10^{-6} m^2 s^{-1} and the lowest average deviation was found between the results of the TDB device and the RUB-TC scanner, that is, 0.2×10^{-6} m^2 s^{-1}.

Deviations in data between the four methods are not systematic for samples with low-to-medium content of anisotropic minerals. For them, the lowest standard deviations were found, that is, 0.06×10^{-6} and 0.07×10^{-6} m^2 s^{-1} for the lower calc-silicate gneiss (C404S2) and the amphibolite sample (C470S4), respectively. For samples with high content of anisotropic minerals, the modified Ångström method systematically yields the lowest and the TPS device the highest α values. For these samples, high standard deviations of all measurements were found, for example, 0.30×10^{-6} and 0.47×10^{-6} m^2 s^{-1} for the granitoid gneiss (C635S5) and the mylonite (C652S1) samples, respectively.

4 DISCUSSION

The application of different methods to investigate thermal properties of reference samples and samples prepared from drill cores of the COSC-1 borehole yielded results that partly exhibit differences exceeding uncertainty estimates. While all three thermal properties,

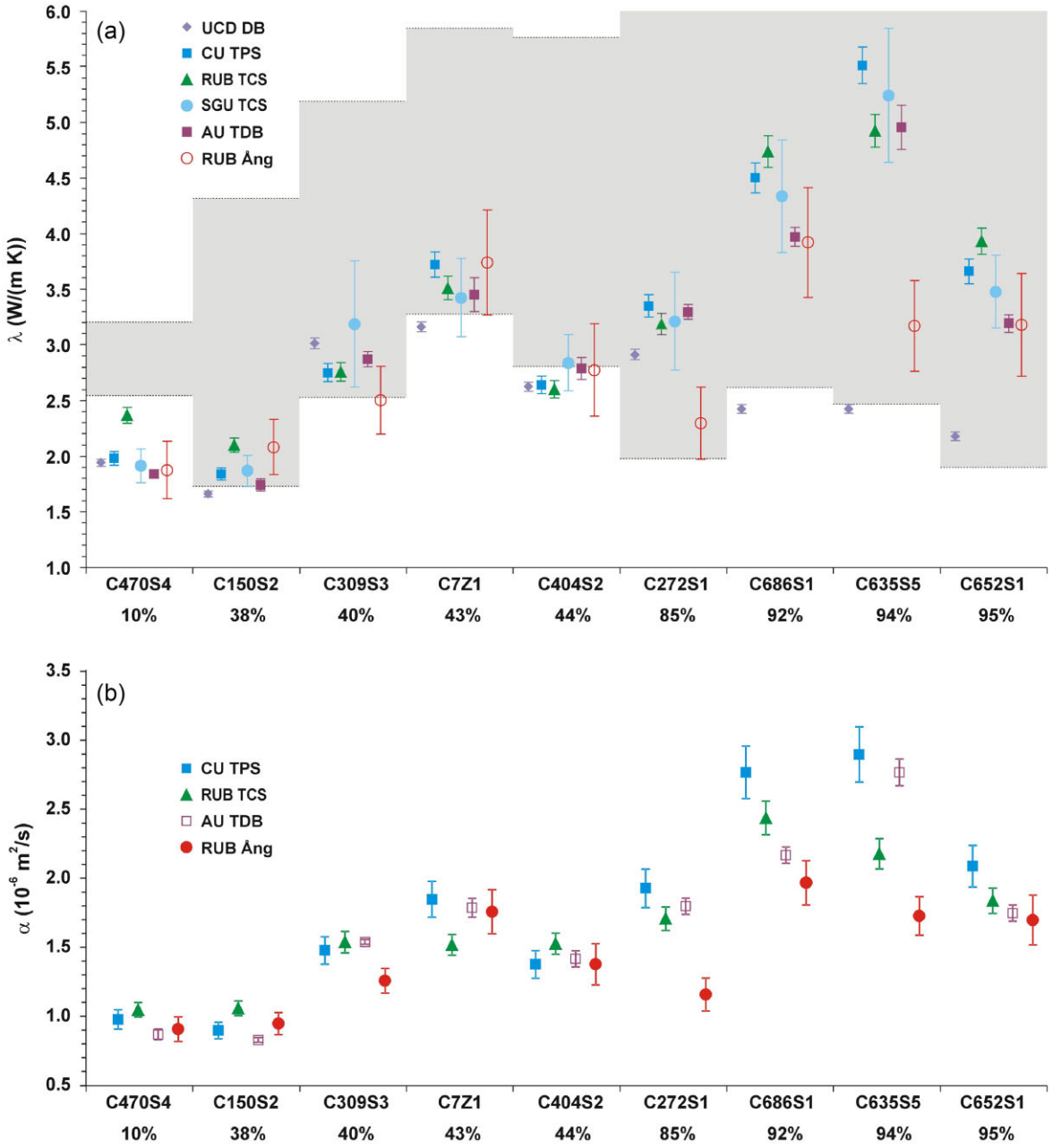

Figure 7. (a) Thermal conductivity λ and (b) thermal diffusivity α for COSC-1 samples determined at the participating laboratories employing steady-state divided bar (DB), transient divided bar (TDB), transient plane source (TPS), modified Ångström and two optical thermal conductivity scanners (TCS). Combined volume fractions of the anisotropic minerals, quartz and mica, are given in (vol per cent). Solid symbols indicate that λ or α were measured directly. All values but the results of the steady-sate divided bar method (DB) do not represent specific tensor components but are derived assuming isotropy; specifics of the measurement geometries are given in Table 2. In (a), the grey areas represent the conductivities calculated based on mineral contents according to the Voigt and Reuss averages (2, 3). Solid symbols indicate that α was measured directly.

specific heat capacity c_p, thermal conductivity $\boldsymbol{\lambda}$ and thermal diffusivity $\boldsymbol{\alpha}$ are affected by the mineralogical composition, the scalar property c_p depends only on the volume fractions of components. The two tensorial properties, $\boldsymbol{\lambda}$ and $\boldsymbol{\alpha}$, also depend on the shape and spatial arrangement of minerals forming a rock, that is, its (micro-) structure, adding to the potential causes for differences in results from different methods.

For the investigated materials, the variability in thermal diffusivity is dominated by the differences in their thermal conductivity, covering up to a factor of three compared to the specific heat capacity values that differ by at most 30 per cent. Thus, a separate discussion of the results for thermal diffusivity is hardly warranted, but the main observations for thermal conductivity also hold for it. The results of the employed thermal scanners, however, entail an additional complexity, because temperature transients measured in two orthogonal directions are evaluated, a technical peculiarity that may lead to a more critical role of the curvature of the scanned surfaces for the determination of α than that for λ.

4.1 Role of sample-to-sample variability and differences in test conditions

Sample-to-sample variability is a complicating issue of our interlaboratory testing, presumably less so for the reference materials than for the samples from the COSC-1 cores. The close consistency of the thermal-conductivity results for two of the presumably isotropic reference materials, Carrara marble and Westerly granite, confirm the general suitability of the methods. The selection of COSC-1 cores for homogeneity based on thermal scanning (e.g. Fig. 1) is supported by the consistency of the results of the density measurements and of the thermal scanning of cores and samples, with the pegmatite as an expectable exception (Fig. A6). Yet, the latter is not among the materials, for which the results of the various methods differ the most.

For six of the nine sets of samples prepared from COSC-1 cores, results of the included methods for thermal conductivity agree to within ± 10 per cent. Thus, it may be concluded that differences in mean temperature, pressure and applied stress (Table C1) inherent to the various methods are unlikely to be the major sources for differences between their results. We cannot exclude, however, that the quartz-dominated composition (> 70 per cent) shared by the three 'problematic' rocks may bias the effects of these state variables and the effects of thermal resistance across the suite of samples. Löwe (2020) investigated the temperature dependence of thermal diffusivity with the modified Ångström method for 28 samples from the COSC-1 borehole, including 8 from this interlaboratory comparison, in the range of $-10\,^{\circ}$C to $60\,^{\circ}$C, and found decreases of 0.25 to 0.5 per cent K^{-1} in good agreement with previous studies (e.g. Clauser 2011a). This modest temperature dependence is likely insufficient to explain the differences of more than 10 per cent between the results of the various methods for some samples. Yet, the temperature dependence of conductivity and diffusivity in principle leads to nonlinearity of the diffusion equation underlying the evaluation of transient temperature records. An investigation of the implications of this additional complexity is beyond the scope of this paper.

4.2 Reproducibility and limits of methods

In cases, reproducibility may be insufficiently reflected in currently reported uncertainty values, as indicated by the repeat measurements 2016 and 2017 on three samples with the transient-divided bar approach (Renner & Pascal 2024). The close match between results from thermal scanning of cores and samples at RUB (Appendix G), in contrast, indicates generally good reproducibility (Fig. A6), the observations for the pegmatite evidencing the pitfalls of sample heterogeneity for our comparative approach.

The exceptional thermal properties of the Al_2O_3 ceramic seem to exceed the technical limits of some methods. In particular, the scanning of the cylinder sidewall by the RUB-team did not provide interpretable temperature profiles. However, scanning of the flat end faces conducted at SGU provided a plausible λ value, highlighting the importance of surface curvature for scanner results.

4.3 Relation between experimental results and calculated effective properties

For specific heat capacity, we find good consistency between the calorimetric approach using Dewar flasks and the predictions according to Kopp's law (1) (Fig. 6d). Yet, the uncertainty of the experimental determinations is about twice as large as the nominal one of the theoretical calculations. Clearly, it should be an aim of experimentalists to improve the accuracy of calorimetric measurements on rock samples. The quality of calculations of specific heat capacity based on Kopp's law (1) will probably often suffice, given that specific heat capacity of minerals exhibits limited variations anyway, but will critically depend on representative compositional analyses as well as reliable input data for, for example, solid-solution series. The current data set does not allow us to comment on the quality of input parameters used in our application of Kopp's law.

Of the transient methods providing specific heat capacity, the results gained with transient-divided bar device exhibit the closest correspondence with the calorimetric results. The correspondence is slightly poorer for the transient plane source approach and thermal scanning. For the latter, the largest discrepancy is observed for two of the samples with the largest amount of anisotropic minerals, and it is obvious that specific heat determination from thermal scanning is generally not reliable for anisotropic samples because of the geometry of the temperature measurements.

The most rigorous bounds estimated for thermal conductivity of COSC-1 samples, based on the well-known averaging schemes (2, 3), are generally wide apart, that is, a factor of two or more, but for the amphibolite (C470S4, Table 4, for which all methods, in addition, suspiciously yield results below the lower bound (Fig. 7a), possibly indicating poor input data for the calculations, with that for amphibole probably the prime suspect. The thermal conductivity gained from steady-state divided bar measurements is the lowest in five out of nine cases and then also just below the estimated lower bound. Three out of these five cases are related to the rocks that contain the most anisotropic minerals. In the light of the moderate foliation dips, the steady-state divided bar measurements suggest, at face value, that thermal conductivity is less perpendicular to foliation than within foliation planes, for these rocks. Furthermore, the λ values determined with the steady-state DB are generally in good agreement with the 'extreme' Reuss bound for anisotropic layering, representing transport across layers composed of minerals whose least conductive crystal axes are aligned with the normal to the layering, especially for the samples with the highest amounts of anisotropic minerals (Fig. 7). Thin section analysis revealed that the b-axis of mica minerals are preferentially oriented normal to the foliation (Fig. 2) as assumed for the calculation of the extreme Reuss bound but neither sorting nor preferred orientation of minerals seem to be so prominent as assumed for the calculation of the extreme bound, and other reasons for the relative low conductivity values of the steady-state divided bar method should not be discounted.

The general tendency for results of, judging from their content of anisotropic minerals and the absence of pronounced layering, presumably isotropic samples to be close to the calculated extreme lower bounds may point towards a conductivity decreasing contribution of microfractures that are not accounted for in the calculations. Poor quality of input data for the averaging schemes seems a less likely cause for this systematic relation between experimental results and bounds, because of the wide variability of the samples' composition. A significant role of microfractures for the conductivity of COSC-1 cores is further supported by the observations on the effect of saturation (Fig. 3).

4.4 Role of thermal anisotropy

Aspects of the deviations between the different measuring approaches seem to be systematically affected by sample anisotropy, as also indicated by the pyrophyllite reference (Figs 4, 5). The

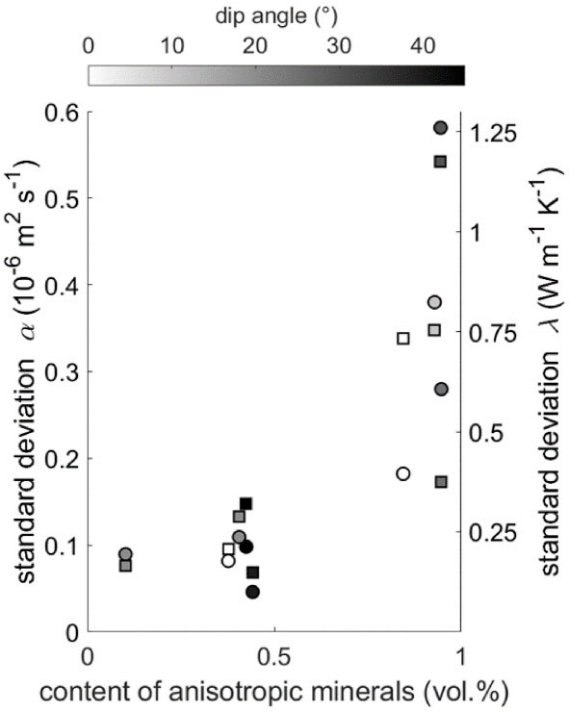

Figure 8. Correlations between the standard deviation of thermal diffusivity α (squares, left axis) and thermal conductivity λ (circles, right axis) of the comparative measurements performed in this study and content of anisotropic minerals (Table E1). Approximate dips of foliation (Table 4) are indicated by the colour coding.

largest standard deviations of thermal conductivity are observed for COSC-1 samples with the highest content of anisotropic minerals, that is, C272S2, C635S5, C652S1 and C686S1 (Figs 6, 7, 8). It may be of relevance, that the three samples with the highest content of anisotropic minerals also exhibit the largest mean conductivity values (Fig. 7a). Furthermore, these three samples are the ones from the small core diameter of only 47 mm, that is, less than the diameter of 60 mm recommended by the manufacturer of the optical scanning system (TCS), and thus possibly causing a bias for the results of the optical scanning of sidewalls performed at RUB. We cannot exclude a difference in microfracture density between large and small cores due to a size effect on the stress relaxation the cores experience after their recovery.

The various methods are not expected to give identical results for anisotropic samples, according to theoretical considerations (Appendix A2). The steady-state divided bar apparatus measures the temperature drop over the entire sample, and thus such tests uniquely constrain the thermal conductivity of a sample in the direction of the temperature gradient. If the orientation of the foliation determines the principal axes of the conductivity tensor and the COSC-1 samples can be modelled as transversely isotropic materials, a steady-state DB result corresponds to the cylindrical samples' axial thermal conductivity $\lambda^{\mathrm{ti}}_{\mathrm{axial}}$ related to the principal values of the conductivity tensor as (see A17)

$$\lambda^{\mathrm{ti}}_{\mathrm{axial}} = \left(\lambda_\perp - \lambda_\parallel\right)\cos^2\gamma + \lambda_\parallel \quad , \tag{5}$$

where γ denotes the angle between the direction of the temperature gradient in the DB device and the orientation of $\lambda_\parallel$, here identical to the dip angle (Table 4). The difference between (5) and the proposed upper bound for slender samples (see Table A1), is not significant, on the level of experimental accuracy. In the range of dip angles of the COSC-1 cores ($\lesssim 45^\circ$), the thermal conductivity gained from the steady-state divided bar does not underestimate $\lambda_\perp$ of a transversely anisotropic medium by more than about 30 per cent for $0.5 < \lambda_\perp/\lambda_\parallel < 1$ and likewise does not overestimate $\lambda_\perp$ by more than about 30 per cent for $1 < \lambda_\perp/\lambda_\parallel < 2$ (Fig. A2a).

In the absence of principal conductivity values, we normalize the results of the transient methods by that of the steady-state DB method. The normalized values of the modified Ångström method exceed 1 (Fig. 9a) and are thus implausibly large in the light of the predictions of the analytical relations for apparent thermal conductivities (Fig. A2a). For the thermal scanning, the range of normalized values (Figs 9b, c, d) corresponds to anisotropy ratios $\lambda_\perp : \lambda_\parallel$ of 1:2 to 1:3 (Figs A2c, d) and is thus not obviously suspicious but inconsistencies with the theoretical relations become apparent when cross-correlating those of two methods (Figs 9b, d).

The results from the modified Ångström method and optical scanning at SGU and RUB in two different directions (Table 2), representing averaged radial and axial measurements, respectively, do not exhibit the expected correlations for thermally transversely anisotropic materials (Figs A2b, d). The thermal scanning results agree within about 10 per cent for the majority of samples (Fig. 9d), though they should differ significantly for either anisotropy case, that is, $\lambda_\perp < \lambda_\parallel$ or $\lambda_\perp > \lambda_\parallel$ (Fig. A2d). The results for pyrophyllite are, however, at least qualitatively consistent with less efficient heat conduction in axial than in radial direction, as indicated by the plane-source method, too. A set of optical scanning measurements at RUB on six further cores from COSC-1 (Appendix H), in which scan lines were performed every 45° on the cylinder walls and on the two end faces, excludes sample-to-sample variability and interlaboratory discrepancies and still the variability in thermal-conductivity results are not easily explained by transverse isotropy alone.

The TPS results and that of thermal scanning at SGU exhibit the closest consistency among all methods (Fig. 9c). These two methods also yield higher conductivity values than those of the steady-state DB for pyrophyllite and the COSC-1 samples with high fractions of anisotropic minerals. For the transient plane source method, an analytical relation for apparent conductivity of a transversely material is only known for the specific case, when the source lies in the plane of isotropy. This relation is consistent with the corresponding limit of the apparent thermal conductivity for the averaged radial thermal scans (Table A1). The good correspondence between the two methods suggests that the apparent thermal conductivity for TPS obeys similar relations as that for thermal scanning.

Analytical relations for apparent thermal conductivity are not known for the TDB method. Though the measurement setups of TBD and steady-state DB resemble each other most closely among the employed methods, the thermal conductivity results of the TDB significantly exceed the ones from the steady-state DB for pyrophyllite and COSC-1 samples with large fractions of anisotropic minerals (Fig. 9a), highlighting the need for a recipe for apparent thermal conductivity determination for TDB.

Correlations between transport properties of rocks in general and their anisotropy in particular have been documented previously (e.g. Popov *et al.* 2011; Kim *et al.* 2012). It seems likely that anisotropy in the thermal properties of the COSC-1 samples contributes substantially to the observed differences between the results of the various methods. The foliation of the COSC-1 samples appears to be a prime candidate for the origin of the anisotropy in their physical properties, but a significant contribution by systematically aligned microfractures cannot be ruled out.

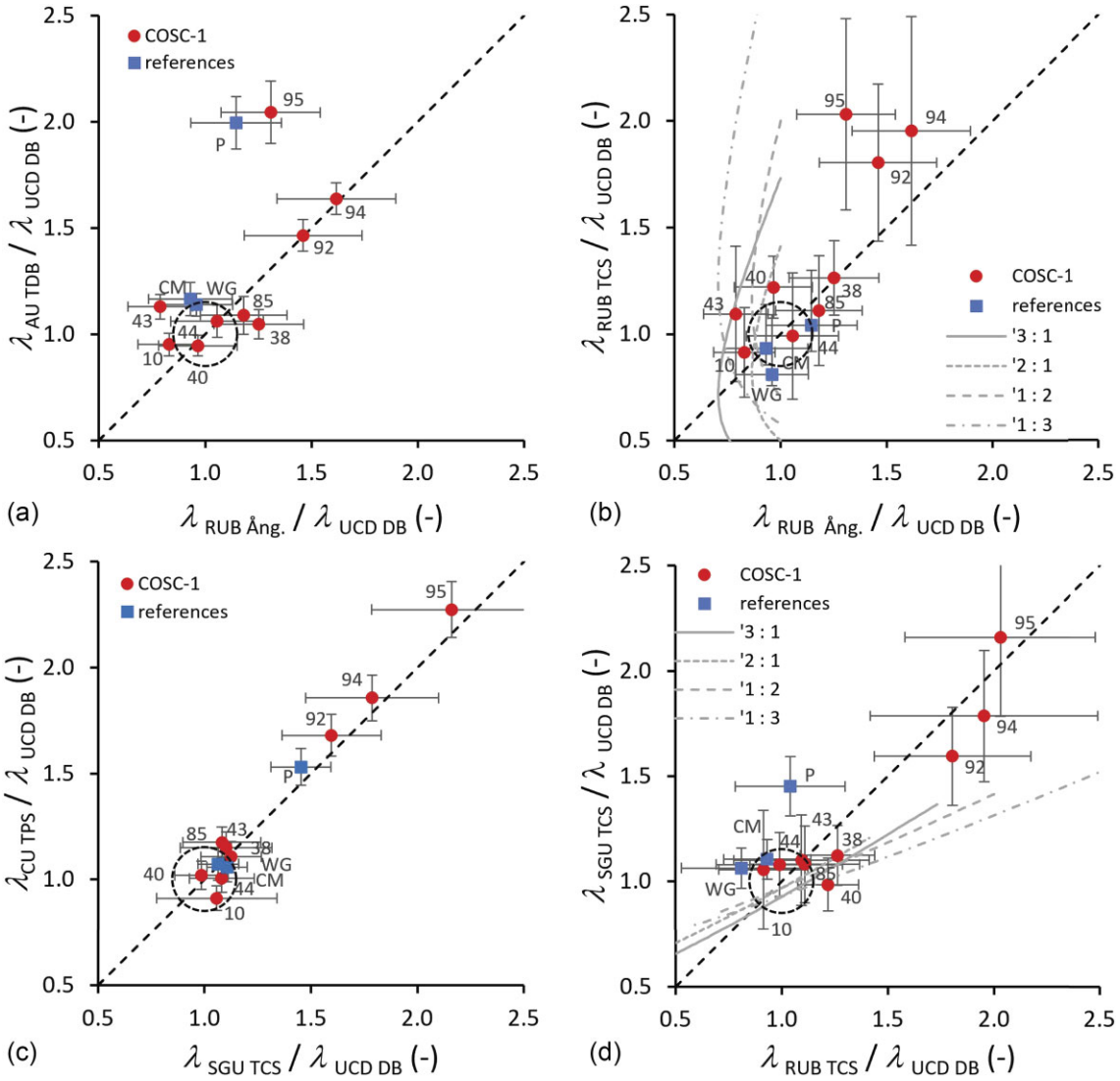

Figure 9. Cross-correlations of thermal conductivities determined with the various methods employed, normalized by the results from the steady-state divided-bar measurements, the supposed benchmark: (a) transient divided bar at AU and modified Ångström at RUB (two axial configurations), (b) optical scanner and modified Ångström at RUB (two axial configurations), (c) transient plane source at CU and optical scanner at SGU (two radial configurations) and (d) the two optical scanners (radially averaged at SGU, axial at RUB). The fractions of anisotropic minerals in COSC-1 samples are indicated by the numbers next to the symbols; the acronyms indicate the three reference materials, P pyrophyllite, CM Carrara marble and WG Westerly granite. The dotted circles indicate the regions, for which the different results would agree within 10 per cent with each other and the steady-state divided-bar results. The dashed straight line represents 1 : 1 agreement. The grey lines in (b) and (d) represent the theoretical relations for transversely isotropic materials covering dip angles from 0 to $\pi/2$ (see Table A1); their labels indicate the anisotropy ratio $\lambda_\perp/\lambda_\parallel$.

4.5 Effect of microfractures: saturation and mechanical loading

The investigation of samples in different saturation states provides some constraints on the potential significance of microfractures and the variability of their water content for the thermal properties of the as-delivered samples, for which the largest data set was collected. The increase in thermal conductivity due to saturation remains restricted to about 25 per cent (Fig. 3a), that is, variable water content of as-delivered samples cannot account for the differences of a factor of two observed for some combinations of samples and methods.

The sheer magnitude (up to 25 per cent) of the changes in thermal conductivity associated with water saturation of samples, as derived from steady-state divided-bar measurements, is, however, somewhat surprising, given the low porosity values of the sample suite (Fig. 3a). This sensitivity to water saturation indicates that the porosity is due to microfractures rather than equant voids. The apparent anticorrelation of porosity and increase in thermal conductivity due to water saturation, as determined by the steady-state divided-bar method (Fig. 3a), is at odds with theoretical expectations (see Section 2.3) and typical trends (e.g. Clauser 2011b), and may be simply owed to the restricted range in porosity and the heterogeneous sample suite but may also be an indication of the complex influence of microfractures on thermal conductivity.

Saturating fractures with water has a comparable effect on thermal conductivity as closing them mechanically. In either case, the conductivity-decreasing effect of empty voids is reduced (Walsh & Decker 1966). Thus, the observed differences between dry and saturated samples also provides a constraint on the maximum effect of differences in mechanical loading to which the samples are

subjected in the various methods (Table 2). It should, however, be stressed that differences in the saturation and mechanical state of microfractures may have a complex effect on anisotropy of samples (e.g. Du *et al.* 2023), and thus on differences among the results of the employed methods. The difference in observations regarding the effect of water-saturation between the steady-state and the transient divided-bar methods are striking. We cannot exclude a contribution from thermal resistance between the assembly interfaces, which may account for an uncertainty of up to 4 per cent and about 10 per cent in thermal conductivity and thermal diffusivity, respectively, with the latter being consistently underestimated if the effect of thermal resistance is not accounted for (Bording *et al.* 2016). A potential effect of saturation on thermal resistance has not yet been explored. The magnitude of the differences between the conductivity results of the two divided-bar approaches seems, however, to underline the variability of the response of heterogeneous media to different thermal perturbations.

We derive a significant conductivity-reducing contribution of microfractures from the relation between aggregate and crystal data for Carrara marble, too. Our results for the thermal conductivity of dry samples of Carrara marble, closely consistent with previously reported ones (Vretenár *et al.* 2007), fall significantly below even the lowest mineral conductivity reported for calcite (Table F1; Birch & Clark 1940). Carrara marble has been reported to exhibit a modest preferred orientation of crystals (Pieri *et al.* 2001), but the potential for anisotropy due to crystallographic-preferred orientations in calcite aggregates is limited since the difference between the thermally least and best conductive direction in calcite is at most 15 per cent (Table F1; Birch & Clark 1940), and potentially less in the light of 10 per cent uncertainty in individual values. The role of microfractures for anisotropy in thermal properties of crystalline rocks should be considered. Microfractures may well serve as an explanation for the observed aggregate conductivity values of the amphibolite samples (C470S4, Fig. 7a), too, falling short of literature values for minerals. Actually, in accord with theoretical treatments (Sevostianov 2006; Nguyen *et al.* 2017; Li *et al.* 2021), the general tendency for conductivity results to fall close to the lower bound (Fig. 7a) may indicate the role of microfractures, rather than the explanation of preferred conduction paths in polyphase rocks advocated by Fuchs et al. (2018).

4.6 Heterogeneity and effectively investigated sample volume

For the transient methods, the imposed thermal-gradient fields vary differently in space and time, and thus the results of measurements on heterogeneous samples will also depend on the thermally perturbed rock volume (Table 2). The spatial scale of structural elements (e.g. layer or foliation thickness, distance between microfractures) will add to a potential scale dependence in addition to grain size. The set of separate optical scanning measurements on six further cores from COSC-1 (Appendix H), in which scan lines were performed every 45° on the cylinder walls and on the two end faces, revealed modest variability of results of axial scans but significant discrepancies among that of radial scans. The limited penetration depth of scans may lead to significantly varying results depending on which layer of a layered material is actually exposed by the surface.

The fundamental lack of analytical relations of effective thermal diffusivities for transient thermal processes (e.g. Carson 2022) means that, for heterogeneous samples, different transient methods may yield different results without one being more or less accurate than the others. Different transient methods simply probe different aspects of heterogeneous structures, as shown for hydraulic properties (Schepp & Renner 2021). A similar analogy is the prominent difference between static and dynamic elastic properties (e.g. Fjær *et al.* 2013). The steady-state divided bar measurements correspond to the quasi-static mechanical measurements, either providing the average over the entire sample volume. In contrast, a transient thermal method's sampling of the network of thermal conductors may be dominated by highly conductive paths, as the stiff components dominate the outcome of dynamic mechanical measurements (e.g. Mukerji *et al.* 1995; Tworzydło & Beenakker 2000). While a contribution from thermal resistance cannot be excluded, our general observation of the least thermal conductivity for the steady-state divided bar method is an indication that heterogeneity plays a role for the observed differences among the methods, which in fact may bear significant information to be revealed by, for example, numerical modelling of the various test approaches for heterogeneous media.

5 CONCLUSIONS

Our interlaboratory comparison of a range of methods commonly employed for the determination of thermal properties of rocks revealed variability of results for selected reference materials and samples prepared from cores of the ICDP COSC-1 borehole, Sweden, that exceeds the methods' nominal uncertainties. Of the three thermal properties, conductivity λ, diffusivity α and specific heat capacity c_p, the latter is the least affected by compositional variations and, as a volumetric property, does not depend on (micro)structure. In itself, c_p is not a quantity that exhibits large variations for minerals (barely a factor of 2); this invariability combined with the typical uncertainty of 10 per cent made it difficult to confirm the significance of differences between various methods and/or of rock types. Kopp's law appears a reliable approach but for cases where uncommon and poorly investigated minerals dominate the composition. Even for the apparently thermally anisotropic samples, the c_p estimates of none of the transient methods are systematically off the others, the results of the transient-divided bar device exhibiting the closest correspondence with the calorimetric results.

The determined structure-dependent transport properties, thermal conductivity and diffusivity, exhibit fair agreement among the methods but not within the quoted uncertainties for the supposedly isotropic samples of Carrara marble and Westerly granite, two of the four selected reference materials. With its extreme thermal conductivity, the aluminium oxide ceramic proved to be a challenge for several methods, but likely not meaning a restriction for testing of rocks. Anisotropy is considered responsible for the spread of the results for the pyrophyllite reference sample. Likewise, the prominent observation for the samples prepared from the nine investigated COSC-1 cores is that the standard deviations of the determinations of thermal properties for a specific sample correlate with its content of anisotropic minerals. This correlation suggests that discrepancies between the results of the various methods are related to the degree of anisotropy of the samples tested. The majority of experimental results do fall within the theoretical bounds for thermal conductivity calculated from mineral volumes determined via thin section analysis and literature values for the mineral properties. However, they do not match with predictions of apparent conductivity for transversely

isotropic materials, and may actually be significantly affected by the presence of microfractures.

The determination of tensor components of the transport properties, thermal conduction and diffusivity, involves the challenge of identifying the orientation of the principal axes for polymineralic rocks. We envision a successive approach involving different methods to be advantageous. Thermal scanning has the advantages of modest sample preparation requirements and of the possibility to investigate a single sample in several directions and thus of providing constraints on the degree of anisotropy and the orientation of principal axes. The small volume investigated by thermal scanning may lead to spurious results and may require a statistical analysis to deduce anisotropy parameters, though (see Kukkonen 2023). Furthermore, thermal scanning does not allow to vary the state of samples (temperature, pressure, stress and saturation). Equipped with results from scanning, however, one can prepare samples in the assumed directions of principal axes to be tested by another method suitable for tests at controlled conditions, of which the steady-sate divided bar approach exhibits benchmark character. The issue of thermal resistance inherent in this method is diminished when samples are mechanically loaded. Finally, combining methods may help to understand and characterize the role of sample heterogeneity for thermal laboratory experimentation. This potential can, however, only be unlocked if rigorous uncertainty analyses are performed for each method.

A clarification of the transient methods' potential for constraining tensor components requires an interlaboratory test on an anisotropic material, for which sample-to-sample variability can be better excluded than for the COSC-1 cores. Such an endeavour should also aim for uniform saturation state of samples. The spatial scales of heterogeneity and anisotropy (e.g. grain size, layer thickness) should be recognized by microstructural investigations, and comprehensive numerical modelling for the various set-ups should accompany such an effort. The latter should also be employed to assess whether and how sample anisotropy affects lateral heat losses and/or the realization of constant-temperature boundary conditions, key aspects of the steady-state divided bar method considered the benchmark-providing approach for thermal conductivity components. Clarifying the role of heterogeneity for transient heat conduction remains of paramount importance for future research. We expect that advancements on sample scale gained from cross-checking experimental observations and numerical models will yield recipes for *in-situ* measurements, characterized by sparse information on elements of heterogeneity, and also for modelling on the scale of metres to hundreds of metres.

In the light of the specific modelling task at hand in the COSC-1 project, the focus of our study was on low-porosity metamorphic rocks. The effect of microfractures on the conductivity and diffusivity results, evidenced by the observations on the effect of water saturation but also the general relation between mineral and aggregate data, may serve as a general note of caution regarding the practice of uncritically using laboratory results in modelling of *in-situ* observations. *In-situ*, the effect of microfractures will likely be diminished due to saturation and mechanical loading. It appears of paramount importance to expand testing under controlled stresses. Realistically, basing thermal modelling on input parameters derived from laboratory experiments should not consider uncertainties quoted of individual methods but probably at least 10 per cent. Furthermore, the effect of transversal isotropy should be explored for specific formations with an anisotropy factor of up to about 2, our suite of experiments suggesting that thermal conductivity is less perpendicular to foliation than within foliation planes.

ACKNOWLEDGMENTS

The authors thank the International Continental Scientific Drilling Program (ICDP), the Swedish Scientific Drilling Program (SSDP) and German Research Foundation (DFG) for providing the core material and funding. Moreover, we thank the International Geothermal Centre Bochum (now Fraunhofer Research Institution for Energy Infrastructures and Geothermal Systems IEG) for granting access to their TC scanner. We thank Ilmo Kukkonen for initiating the interlaboratory comparison. Nino Block is gratefully acknowledged for scanning the COSC cores before selecting the ones from which samples were prepared for this study. The first author is grateful to Thomas Andolfsson for his help with the Ångström method. The presented work is part of the PhD thesis of RL financed by DFG grant PA1730/3 in the framework of SPP 1006 (ICDP). We gratefully acknowledge the constructive comments of Ilmo Kukkonen and three anonymous reviewers.

DATA AVAILABILITY

The data created in the course of this interlaboratory study are compiled in Renner & Pascal (2024) at https://doi.org/10.5281/zenodo.11141628.

REFERENCES

Andolfsson, L.T.G., 2019. *Thermal Properties of Rocks: A Periodic Solution of Thermal Diffusion and Its Application to the Pressure Dependency of Thermal Properties, PhD Thesis,* Ruhr-Universität Bochum.

Andreescu, M., Nielsen, S.B., Polonic, G. & Demetrescu, C., 2002. Thermal budget of the Transylvanian lithosphere. Reasons for a low surface heat-flux anomaly in a Neogene intra-Carpathian basin, *Geophys. J. Int.,* **150**(2), 494–505.

Ångström, A.J., 1862. Neue Methode, das Wärmeleitungsvermögen der Körper zu bestimmen, *Ann. Phys.,* **190**(12), 513–530.

Beardsmore, G.R. & Cull, J.P., 2001. *Crustal Heat Flow: A Guide to Measurement and Modelling,* Cambridge Univ. Press.

Beck, A.E., 1988. Thermal properties, in *Handbook of Terrestrial Heat-Flow Density Determination: with Guidelines and Recommendations of the International Heat-Flow Commission, Solid Earth Sciences Library,* pp. 87–165, eds Haenel, R., Rybach, L. & Stegena, L., Springer Netherlands.

Birch, A.F. & Clark, H., 1940. The thermal conductivity of rocks and its dependence upon temperature and composition, *Am. J. Sci.,* **238**(8), 529–558.

Birch, F., Schairer, J.F. & Spicer, H.C., 1942. *Handbook of Physical Constants,* Geological Society of America.

Block, N., Renner, J. & Pascal, C., 2024. *Measurement of thermal properties of core samples from the COSC-1 borehole*. Available thanks to GFZ Data Services at https://dataservices.gfz-potsdam.de/icdp/showshort.php?id=68f2772b-88a6-11ef-967a-4ffbfe06208e.

Bording, T.S., Nielsen, S.B. & Balling, N., 2016. The transient divided bar method for laboratory measurements of thermal properties, *Geophys. J. Int.,* **207**(3), 1446–1455.

Brigaud, F., Chapman, D.S. & Douaran, S.L., 1990. Estimating thermal conductivity in sedimentary basins using lithologic data and geophysical well Logs1, *AAPG Bull.,* **74**(9), 1459–1477.

Brigaud, F., Vasseur, G. & Caillet, G., 1992. Thermal state in the North Viking Graben (North Sea) determined from oil exploration well data, *Geophysics,* **57**(1), 69–88.

Bullard, E.C. & Day, A., 1961. The Flow of Heat through the Floor of the Atlantic Ocean, *Geophys. J. Int.,* **4,** 282–292.

Carslaw, H.S. & Jaeger, J.C., 1959. *Conduction of Heat in Solids,* Clarendon Press, 2nd edn.

Carson, J.K., 2022. Modelling thermal diffusivity of heterogeneous materials based on thermal diffusivities of components with implications for thermal diffusivity and thermal conductivity measurement, *Int. J. Thermophys.,* **43**(7), 108.

Carte, A.E., 1955. Thermal constants of pyrophyllite and their change on heating, *British J. Appl. Phys.,* **6**(9), 326.

Cermak, V. & Rybach, L., 1982. Thermal properties: thermal conductivity and specific heat of minerals and rocks, in *Landolt-Börnstein Zahlenwerte and Funktionen Aus Naturwissenschaften Und Technik, Neue Serie, Physikalische Eigenschaften Der Gesteine,* Vol. **V/la,** pp. 305–343, ed. Angenheister, G., Springer Verlag.

Cernuschi, F., Ahmaniemi, S., Vuoristo, P. & Mäntylä, T., 2004. Modelling of thermal conductivity of porous materials: application to thick thermal barrier coatings, *J. Eur. Ceramic Soc.,* **24**(9), 2657–2667.

Chen, W. & Decker, D.L., 1992. Pressure dependence of the thermal conductivity of pyrophyllite to 40 kbar, *J. Appl. Phys.,* **71**(6), 2624–2627.

Clauser, C., 2011a. Thermal Storage and Transport Properties of Rocks, II: Thermal Conductivity and Diffusivity, in *Encyclopedia of Solid Earth Geophysics,* pp. 1431–1448, ed. Gupta, H.K., Springer Netherlands.

Clauser, C., 2011b. Thermal storage and transport properties of rocks, I: Heat capacity and latent heat, in *Encyclopedia of Solid Earth Geophysics, Encyclopedia of Earth Sciences Series,* pp. 1423–1431, ed. Gupta, H.K., Springer Netherlands.

Clauser, C. & Huenges, E., 1995. Thermal conductivity of rocks and minerals, in *Rock Physics & Phase Relations,* pp. 105–126, ed. Ahrens, T.J., American Geophysical Union (AGU).

Diment, W.H. & Pratt, H.R., 1988. *Thermal Conductivity of Some Rock-Forming Minerals: A Tabulation, Open-File Report 88-690* , United States Department of the Interior Geological Survey

Du, K., Cheng, L., Barthélémy, J.-F., Sevostianov, I., Giraud, A. & Adessina, A., 2023. Effective thermal conductivity of transversely isotropic materials with concave pores, in *Advances in Linear and Nonlinear Continuum and Structural Mechanics, Advanced Structured Materials,* pp. 115–134, eds Altenbach, H. & Eremeyev, V., Springer Nature Switzerland.

El Yagoubi, J., Lamon, J., Batsale, J.-C. & Le Flem, M., 2019. Experimental assessment of damage-thermal diffusivity relationship in unidirectional fibre-reinforced composite under axial tensile test, *Acta Mater.,* **173,** 302–312.

Fjær, E., Stroisz, A.M. & Holt, R.M., 2013. Elastic dispersion derived from a combination of static and dynamic measurements, *Rock Mech. Rock Eng.,* **46**(3), 611–618.

Frey, M., Bär, K., Stober, I., Reinecker, J., van der Vaart, J. & Sass, I., 2022. Assessment of deep geothermal research and development in the Upper Rhine Graben, *Geotherm. Energy,* **10**(1), 18.

Fuchs, S. & Förster, A., 2014. Well-log based prediction of thermal conductivity of sedimentary successions: a case study from the north German basin, *Geophys. J. Int.,* **196**(1), 291–311.

Fuchs, S., Balling, N. & Förster, A., 2015. Calculation of thermal conductivity, thermal diffusivity and specific heat capacity of sedimentary rocks using petrophysical well logs, *Geophys. J. Int.,* **203**(3), 1977–2000.

Fuchs, S., Förster, H.J., Braune, K. & Förster, A., 2018. Calculation of thermal conductivity of low-porous, isotropic plutonic rocks of the crust at ambient conditions from modal mineralogy and porosity: a viable alternative for direct measurement?, *J. geophys. Res.: Solid Earth,* **123**(10), 8602–8614.

Fuchs, S. *et al.*, 2023. Quality-assurance of heat-flow data: the new structure and evaluation scheme of the IHFC Global Heat Flow Database, *Tectonophysics,* **863,** 229976.

Galson, D.A., Wilson, N.P., Schärli, U. & Rybach, L., 1987. A comparison of the divided-bar and QTM methods of measuring thermal conductivity, *Geothermics,* **16**(3), 215–226.

Grubbe, K., Haenel, R. & Zoth, G., 1983. Determination of the vertical component of thermal conductivity by line source methods, *Zentralbl. Geol. Paläontol.,* **1,** 49–56.

Gustafsson, S.E., 1991. Transient plane source techniques for thermal conductivity and thermal diffusivity measurements of solid materials, *Rev. Sci. Instrum.,* **62**(3), 797–804.

Gustafsson, S.E., Gustafsson, M. & Gustafsson, J., 2000. *Method of measuring thermal properties of materials with direction dependant properties,* World International Intellectual Property Organization, WO 00/70333,

He, Y., 2005. Rapid thermal conductivity measurement with a hot disk sensor: Part 1. theoretical considerations, *Thermochim. Acta,* **436**(1), 122–129.

Heuze, F.E., 1983. High-temperature mechanical, physical and thermal properties of granitic rocks— a review, *Int. J. Rock Mech. Mining Sci. Geomech. Abstr.,* **20**(1), 3–10.

Horai, K.-I., 1971. Thermal conductivity of rock-forming minerals, *J. geophys. Res.,* **76**(5), 1278–1308.

Horai, K.-I. & Simmons, G., 1969. Thermal conductivity of rock-forming minerals, *Earth planet. Sci. Lett.,* **6**(5), 359–368.

Jessop, A.M., 1990. Comparison of industrial and high-resolution thermal data in a sedimentary basin, *Pure appl. Geophys.,* **133**(2), 251–267.

Jorand, R., Vogt, C., Marquart, G. & Clauser, C., 2013. Effective thermal conductivity of heterogeneous rocks from laboratory experiments and numerical modeling, *J. geophys. Res.: Solid Earth,* **118**(10), 5225–5235.

Ramstad, F., Kalskin,, R., Beer,, de, Midttømme,, K., Koziel,, J. & Wissing,, B., 2008. Status of thermal diffusivity equipment–method development 2005-2008 *NGU Report 2008.050* Geological Survey Norway, pp. 41, https://www.ngu.no/en/node/1135

Kim, H., Cho, J.-W., Song, I. & Min, K.-B., 2012. Anisotropy of elastic moduli, *P*-wave velocities, and thermal conductivities of asan gneiss, boryeong shale, and yeoncheon schist in Korea, *Eng. Geol.,* **147–148,** 68–77.

Kohl, T. & Rybach, L., 1996. Thermal and hydraulic aspects of the KTB drill site, *Geophys. J. Int.,* **124**(3), 756–772.

Kubičár, L., Vretenár, V. & Boháč, V., 2008. Study of phase transitions by transient methods, *Solid State Phenom.,* **138,** 3–28. doi:

Kubičár, L., Hudec, J., Fidrikova, D., Dieska, P. & Vitkovic, M., 2015. Effects in monitoring of the thermal moisture regime of cultural objects located in different climate conditions, *Adv. Mater. Res.,* **1126,** 93–98. doi:

Kukkonen, I.T., 2023. *Thermal Properties of Rocks at Olkiluoto: In situ Heat Transfer Experiment—Thermal Conductivity and Diffusivity Measurements of Drill Cores with the Optical Thermal Scanning Method, Working Report 2023-10,* University of Helsinki.

Li, Z.-W., Liu, Y., Mei, S.-M., Xing, S.-C. & Wang, X.-K., 2021. Effective thermal conductivity estimation of fractured rock masses, *Rock Mech. Rock Eng.,* **54**(12), 6191–6206.

Liebel, H.T., Stølen, M.S., Frengstad, B.S., Ramstad, R.K. & Brattli, B., 2011. Insights into the reliability of different thermal conductivity measurement techniques: a thermo-geological study in Mære (Norway), *Bull. Eng. Geol. Environ.,* **71**(2), 235.

Lorenz, H. *et al.*, 2015. COSC-1–drilling of a subduction-related allochthon in the palaeozoic caledonide orogen of Scandinavia, *Sci. Drilling,* **19,** 1–11.

Lubimova, H.A., Lusova, L.M., Firsov, F.V., Starikova, G.N. & Shushpanov, A.P., 1961. Determination of surface heat flow in mazesta (USSR), *Ann. Geophys.,* **14**(2), 157–167. doi:

Löwe, R.H., 2020. *Steady-state vs. transient heat-transfer in the COSC-1 drill hole, central Sweden. PHD thesis,* Ruhr-Universität Bochum.

McDonald, K.R., Dryden, J.R. & Zok, F.W., 2001. Effects of matrix cracks on the thermal diffusivity of a fiber-reinforced ceramic composite, *J. Am. Ceramic Soc.,* **84**(9), 2015–2021.

McGuinness, T., Hemmingway, P. & Long, M., 2014. Design and development of a low-cost divided-bar apparatus, *Geotech. Testing J.,* **37**(2), 230–241.

Meshalkin, Y., Shakirov, A., Popov, E., Koroteev, D. & Gurbatova, I., 2020. Robust well-log based determination of rock thermal conductivity through machine learning, *Geophys. J. Int.,* **222**(2), 978–988.

Middleton, M.F., 1993. A transient method of measuring the thermal properties of rocks, *Geophysics,* **58**(3), 357–365.

Mukerji, T., Mavko, G., Mujica, D. & Lucet, N., 1995. Scale-dependent seismic velocity in heterogeneous media, *Geophysics,* **60**(4), 1222–1233.

Nguyen, S.T., Vu, M.H., Vu, M.N. & Tang, A.M., 2017. Modeling of heat flow and effective thermal conductivity of fractured media: analytical and numerical methods, *J. appl. Geophys.,* **140,** 117–122.

Norden, B., Förster, A., Förster, H.-J. & Fuchs, S., 2020. Temperature and pressure corrections applied to rock thermal conductivity: Impact on subsurface temperature prognosis and heat-flow determination in geothermal exploration, *Geotherm. Energy,* **8**(1), 1.

Norden, B., Bauer, K. & Krawczyk, C.M., 2023. From pilot knowledge via integrated reservoir characterization to utilization perspectives of deep geothermal reservoirs: the 3D model of Groß Schönebeck (North German Basin), *Geotherm. Energy,* **11**(1), 1.

Pascal, C., 2015. Heat flow of Norway and its continental shelf, *Mar. Petrol. Geol.,* **66,** 956–969.

Pascal, C. & Balling, N., 2023. Heat flow of northern Norway, new data and geodynamic implications, *Tectonophysics,* **867,** 230067.

Pasquale, V., Verdoya, M. & Chiozzi, P., 2015. Measurements of rock thermal conductivity with a transient divided bar, *Geothermics,* **53,** 183–189.

Pasquale, V., Verdoya, M. & Chiozzi, P., 2017. *Geothermics, SpringerBriefs in Earth Sciences,* Springer International Publishing.

Pieri, M., Burlini, L., Kunze, K., Stretton, I. & Olgaard, D.L., 2001. Rheological and microstructural evolution of Carrara marble with high shear strain: results from high temperature torsion experiments, *J. Struct. Geol.,* **23**(9), 1393–1413.

Popov, Y. & Mandel, A., 1998. Geothermal study of anisotropic rock masses, *Izvestiya—Physics of the Solid Earth,* **34,** 903–915.

Popov, Y., Berezin, V., Semionov, V. & Korosteliov, V., 1985. Complex detailed investigations of the thermal properties of rocks on the basis of a moving point source, *Izvestiya—Physics of the Solid Earth,* **21**(1), 64–70.

Popov, Y., Romushkevich, R., Korobkov, D., Mayr, S., Bayuk, I., Burkhardt, H. & Wilhelm, H., 2011. Thermal properties of rocks of the borehole Yaxcopoil-1 (Impact Crater Chicxulub, Mexico), *Geophys. J. Int.,* **184**(2), 729–745.

Popov, Y., Beardsmore, G., Clauser, C. & Roy, S., 2016. ISRM suggested methods for determining thermal properties of rocks from laboratory tests at atmospheric pressure, *Rock Mech. Rock Eng.,* **49**(10), 4179–4207.

Popov, Y.A., Pribnow, D. F.C., Sass, J.H., Williams, C.F. & Burkhardt, H., 1999. Characterization of rock thermal conductivity by high-resolution optical scanning, *Geothermics,* **28**(2), 253–276.

Pribnow, D. F.C. & Sass, J.H., 1995. Determination of thermal conductivity for deep boreholes, *J. geophys. Res.: Solid Earth,* **100,** 9981–9994.

Ratcliffe, E.H., 1959. Thermal conductivities of fused and crystalline quartz, *British J. Appl. Phys.,* **10**(1), 22.

Rath, V. & Mottaghy, D., 2007. Smooth inversion for ground surface temperature histories: Estimating the optimum regularization parameter by generalized cross-validation, *Geophys. J. Int.,* **171**(3), 1440–1448.

Ray, L., Chopra, N., Singh, S.P., Hiloidari, S. & Rao, S.E., 2023. Thermal conductivity at elevated temperature, density and geochemical signatures for the massive rhyolites of the Bundelkhand Craton, central India, *Geophys. J. Int.,* **232**(3), 1742–1755.

Renner, J. & Pascal, C., 2024. *Results of interlaboratory testing on COSC-1 cores and reference samples (density, porosity, thermal properties)*. Available at: https://zenodo.org/records/14016574

Robertson, E.C. & Hemingway, B.S., 1995. *Estimating heat capacity and heat content of rocks, USGS Numbered Series 95-622, U.S. Geological Survey*. doi:

Robie, R.A., Hemingway, B.S. & Wilson, W.H., 1976. The heat capacities of copper and of muscovite $KAl_2(AlSi_3)O_10\ (OH)_2$, pyrophyllite $Al_2Si_4O_10(OH)_2$, and illite $K_3(Al_7Mg)(Si_14Al_2)O_40(OH)_8$ between 15 and 375 K and their standard entropies at 298.15 K, *J. Res. U.S. Geol. Surv.,* **4**(6), 631–644.

Rosberg, J.-E. & Erlström, M., 2019. Evaluation of the Lund deep geothermal exploration project in the Romeleåsen Fault Zone, South Sweden: A case study, *Geotherm. Energy,* **7**(1), 10.

Sass, J.H., 1965. The thermal conductivity of fifteen feldspar specimens, *J. geophys. Res.,* **70**(16), 4064–4065.

Sass, J.H., Stone, C. & Munroe, R.J., 1984. Thermal conductivity determinations on solid rock—a comparison between a steady-state divided-bar apparatus and a commercial transient line-source device, *J. Volc. Geotherm. Res.,* **20**(1), 145–153.

Schepp, L.L. & Renner, J., 2021. Evidence for the heterogeneity of the pore structure of rocks from comparing the results of various techniques for measuring hydraulic properties, *Transp. Porous Media,* **136**(1), 217–243.

Schmitt, D.R., Diallo, M.S. & Weichman, F., 2006. Quantitative determination of stress by inversion of speckle interferometer fringe patterns: Experimental laboratory tests, *Geophys. J. Int.,* **167**(3), 1425–1438.

Schön, J., 2015. *Physical Properties of Rocks, Vol. 65 of Earth and Planetary Sciences,* Elsevier, 2nd edn.

Schubnel, A., Benson, P.M., Thompson, B.D., Hazzard, J.F. & Young, R.P., 2006. Quantifying Damage, Saturation and Anisotropy in Cracked Rocks by Inverting Elastic Wave Velocities, *Pure appl. Geophys.,* **163**(5–6), 947–973.

Seipold, U. & Huenges, E., 1998. Thermal properties of gneisses and amphibolites—high pressure and high temperature investigations of KTB-rock samples, *Tectonophysics,* **291**(1), 173–178.

Sevostianov, I., 2006. Thermal conductivity of a material containing cracks of arbitrary shape, *Int. J. Eng. Sci.,* **44**(8), 513–528.

Sibbitt, W.L., Dodson, J.G. & Tester, J.W., 1978. Thermal conductivity of rocks associated with energy extraction from hot dry rock geothermal systems, in *Thermal Conductivity 15,* pp. 399–421, ed. Mirkovich, V.V., Springer US.

Silliman, S.E. & Neuzil, C.E., 1990. Borehole determination of formation thermal conductivity using a thermal pulse from injected fluid, *J. geophys. Res.: Solid Earth,* **95**(B6), 8697–8704.

Sundberg, J. & Hellström, G., 2009. Inverse modelling of thermal conductivity from temperature measurements at the prototype repository, Äspö HRL, *Int. J. Rock Mech. Mining Sci.,* **46**(6), 1029–1041.

Sundberg, J., Kukkonen, I.T. & Hälldahl, L., 2003. *Comparison of Thermal Properties Measured by Various Methods, Tech. Rep. SKB Rapport R-03-18,* Swedish Nuclear Fuel and Waste Management Co.

Tworzydło, J. & Beenakker, C. W.J., 2000. Hierarchical model for the scale-dependent velocity of waves in random media, *Phys. Rev. Lett.,* **85**(3), 674–676.

Vasseur, G., Bernard, P., Van de Meulebrouck, J., Kast, Y. & Jolivet, J., 1983. Holocene paleotemperatures deduced from geothermal measurements, *Palaeogeogr. Palaeoclim. Palaeoecol.,* **43**(3), 237–259.

Vretenár, V., Kubičár, L., Boháč, V. & Tiano, P., 2007. Thermophysical analysis of gioia marble in dry and water-saturated states by the pulse transient method, *Int. J. Thermophys.,* **28**(5), 1522–1535.

Waite, W.F., Stern, L.A., Kirby, S.H., Winters, W.J. & Mason, D.H., 2007. Simultaneous determination of thermal conductivity, thermal diffusivity and specific heat in sI methane hydrate, *Geophys. J. Int.,* **169**(2), 767–774.

Walsh, J.B. & Decker, E.R., 1966. Effect of pressure and saturating fluid on the thermal conductivity of compact rock, *J. geophys. Res.,* **71**(12), 3053–3061.

Waples, D.W. & Waples, J.S., 2004. A review and evaluation of specific heat capacities of rocks, minerals, and subsurface fluids. Part 1: Minerals and nonporous rocks, *Nat. Resourc. Res.,* **13**(2), 97–122.

Zhang, H., Li, Y.-M. & Tao, W.-Q., 2017. Theoretical accuracy of anisotropic thermal conductivity determined by transient plane source method, *Int. J. Heat Mass Transfer,* **108,** 1634–1644.

APPENDIX A: THERMAL CONDUCTION IN SOLIDS

A1 Fundamentals

The heat capacity C (J K^{-1}) describes the proportionality constant between the change in heat content (dQ) and the change in temperature (dT) of a substance

$$\mathrm{d}Q = C\,\mathrm{d}T = m\,c\,\mathrm{d}T = V\,\tilde{c}\,\mathrm{d}T \quad , \tag{A1}$$

where c and $\tilde{c} = \rho c$ denote specific heat capacity referring to mass and volume, respectively, the latter often addressed as thermal capacity (e.g. Waples & Waples 2004). The temperature change can take place under two endmember–boundary conditions, constant pressure or constant volume, and accordingly isobaric (c_p) and isochoric (c_V) specific heat capacities are distinguished.

The thermal conductivity tensor $\boldsymbol{\lambda}$ (W m^{-1} K^{-1}) reflects the proportionality between conductive heat flux $\mathbf{q}$ and temperature gradient $\boldsymbol{\nabla} T$ in a steady-state regime, as expressed by Fourier's law (e.g. Carslaw & Jaeger 1959):

$$\mathbf{q} = -\boldsymbol{\lambda}\boldsymbol{\nabla} T \quad , \tag{A2}$$

the minus sign indicating that heat flows in the direction of decreasing temperature. Accounting for energy (heat) conservation yields

$$-\boldsymbol{\nabla}\cdot\mathbf{q} = \rho\,c\,\frac{\partial T}{\partial t} \quad , \tag{A3}$$

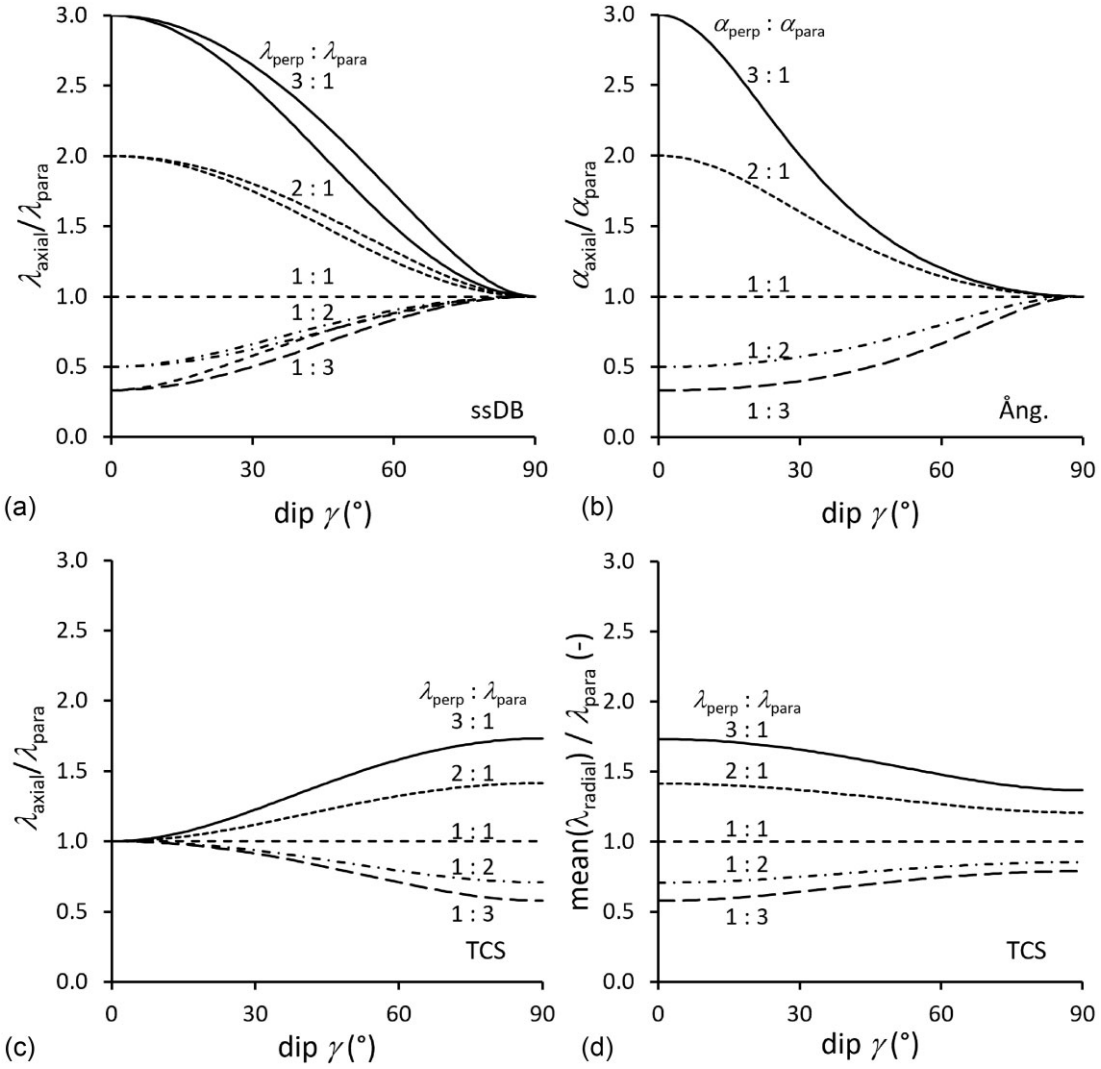

Figure A1. Theoretical predictions of normalized apparent thermal conductivity λ or diffusivity α for measurements on cores in axial or radial direction as a function of the dip angle of the plane of isotropy, that is, angle between core axis and normal to plane of isotropy: (a) steady-state divided bar (upper and lower bound), (b) modified Ångström, (c) axial optical scanning and (d) mean of two orthogonal radial optical scans. The analytical relations are given in Table A1. The curves are labelled by the anisotropy ratio $\lambda_\perp/\lambda_\parallel$ or $\alpha_\perp/\alpha_\parallel$.

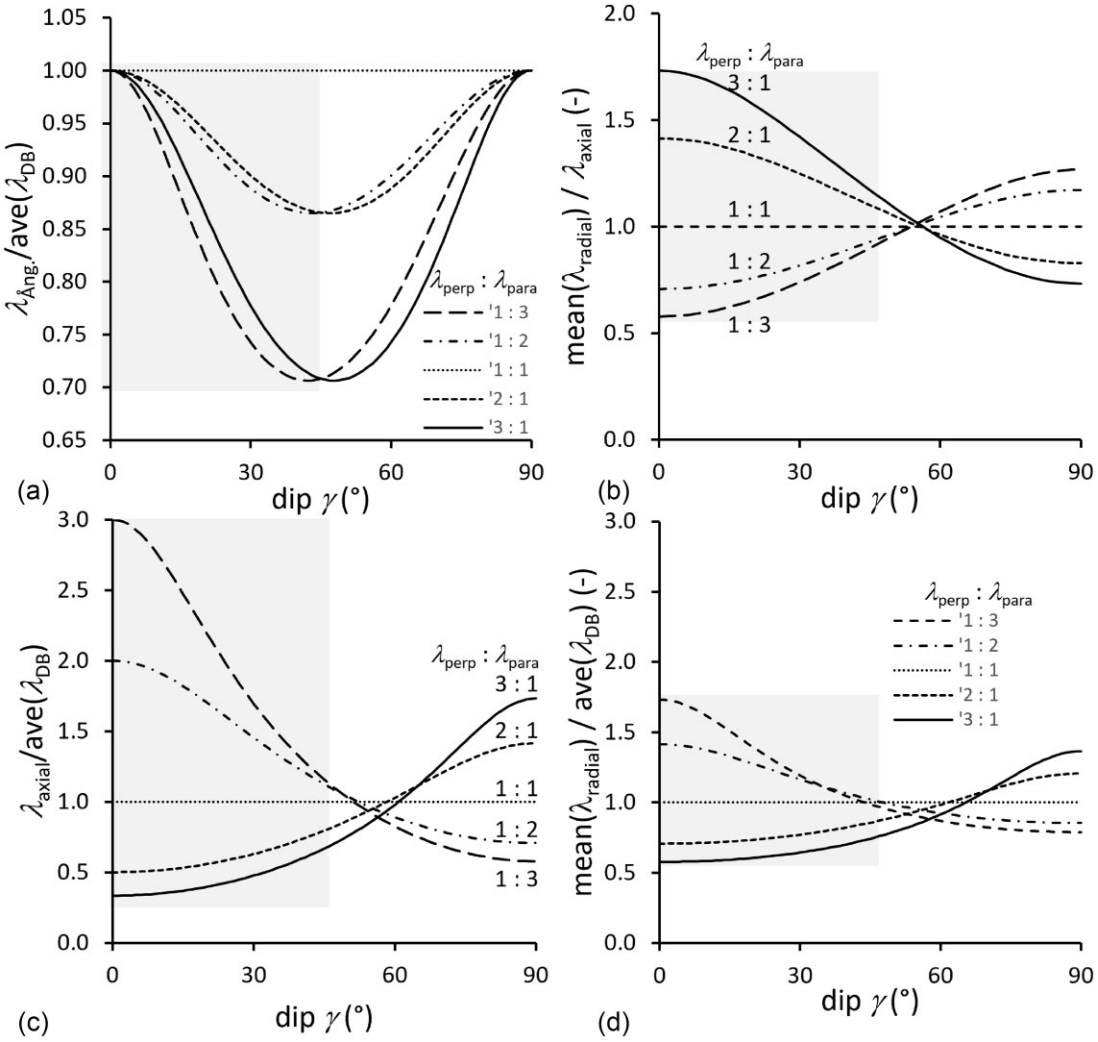

Figure A2. Ratios between apparent thermal conductivities as measured on cores in axial or radial direction as a function of the dip angle of the plane of isotropy, that is, angle between core axis and normal to plane of isotropy: (a) modified Ångström, (b) mean of two orthogonal radial optical scans and (c) axial optical scan to the average of upper and lower bound for steady-state divided bar, see Fig. A1. (d) Ratios between apparent thermal conductivities as gained from the mean of two orthogonal radial and an axial optical scan. The analytical relations are given in Table A1. The curves are labelled by the anisotropy ratio $\lambda_\perp/\lambda_\parallel$ or $\alpha_\perp/\alpha_\parallel$. Note the significantly varying vertical scales.

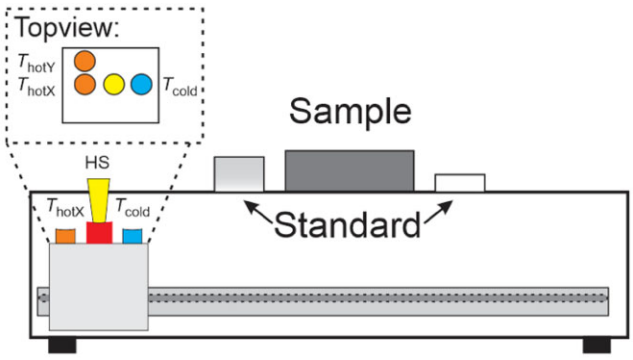

Figure A3. TC scanner with top view onto sensors and heat source (HS) configuration.

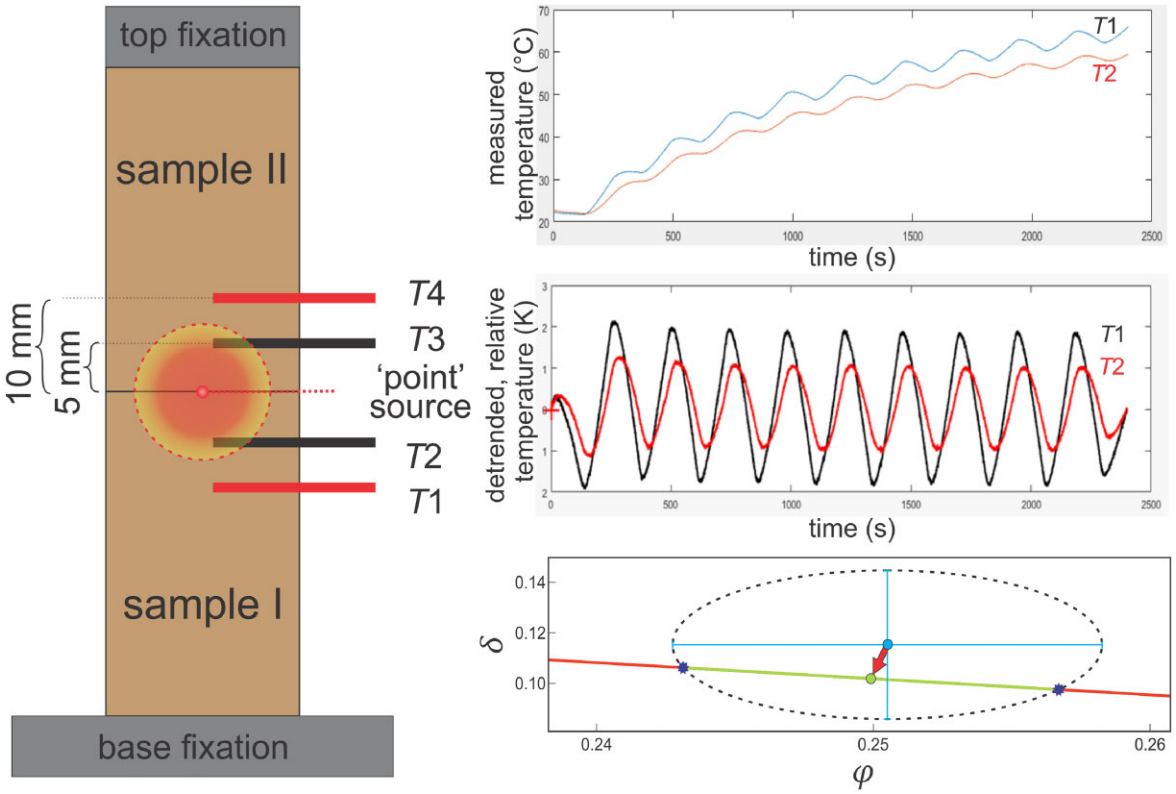

Figure A4. left: Schematic setup of the modified Ångström device (left) with four temperature sensors (T1 to T4). (right from top to bottom) Typical temperature readings versus time and derived detrended, relative temperature time-series. and amplitude ratio δ versus phase shift φ (circle) with corresponding error ellipse (dashed line). The section of the theoretical relation (B4) for a point source falling within the error ellipse is given as the line segment between the stars; results are reported by the midpoints (indicated by arrow) using the distance of these to the end of the segments as uncertainty.

that is, heat in- and outflow (left side) balance with changes in stored heat (right side). Substituting (A2) into (A3) and assuming constant thermal conductivity leads to a diffusion equation for temperature

$$\boldsymbol{\lambda} : \boldsymbol{\nabla} \otimes \boldsymbol{\nabla} T = \rho\, c\, \frac{\partial T}{\partial t} \quad . \tag{A4}$$

Table A1. Apparent thermal conductivity λ_{app} of transversely isotropic materials characterized by $\lambda_\perp$ and $\lambda_\parallel$ gained from the employed methods. The angle γ denotes the angle between the normal to the plane of isotropy and the core axis; the rotation angle θ is defined relative to the strike of the foliation.

Method	Relation
divided bar[1] (DB)	$\lambda_\parallel + \left(\lambda_\perp - \lambda_\parallel\right)\cos^2\gamma \le \lambda_{\mathrm{app}} \le \sqrt{\lambda_\parallel^2 + \left(\lambda_\perp^2 - \lambda_\parallel^2\right)\cos^2\gamma}.$
modified Ångström[2] (Ång.)	$\dfrac{1}{\alpha_{\mathrm{app}}} = \dfrac{1}{\alpha_\parallel} + \left(\dfrac{1}{\alpha_\perp} - \dfrac{1}{\alpha_\parallel}\right)\cos^2\gamma$
TC scanner[3] (TCS)	$\lambda_{\mathrm{app}}^{\mathrm{axial}}(\gamma) = \sqrt{\lambda_\perp\lambda_\parallel + \left(\lambda_\parallel^2 - \lambda_\perp\lambda_\parallel\right)\cos^2\gamma}$ $= \begin{cases} \lambda_\parallel \text{ for } \gamma = 0, & \text{scan line perpendicular to planes of isotropy} \\ \sqrt{\lambda_\perp\lambda_\parallel} \text{ for } \gamma = \pi/2, & \text{scan line in plane of isotropy} \end{cases}$
	$\bar{\lambda}_{\mathrm{app}}^{\mathrm{radial}}(\gamma) = \dfrac{\lambda_{\mathrm{app}}^{\mathrm{radial}}(\gamma,\theta_1) + \lambda_{\mathrm{app}}^{\mathrm{radial}}(\gamma,\theta_1+\pi/2)}{2}$ $= \dfrac{\sqrt{\lambda_\perp\lambda_\parallel + \left(\lambda_\parallel^2 - \lambda_\perp\lambda_\parallel\right)\sin^2\gamma\sin^2\theta_1} + \sqrt{\lambda_\perp\lambda_\parallel + \left(\lambda_\parallel^2 - \lambda_\perp\lambda_\parallel\right)\sin^2\gamma\cos^2\theta_1}}{2}$ $= \dfrac{\sqrt{\lambda_\perp\lambda_\parallel} + \sqrt{\lambda_\perp\lambda_\parallel + \left(\lambda_\parallel^2 - \lambda_\perp\lambda_\parallel\right)\sin^2\gamma}}{2}$ for $\theta_1 = 0, \pi/2$
transient plane source[4] (TPS)	$\lambda_{\mathrm{app}} = \sqrt{\lambda_\perp\lambda_\parallel}$ and $\alpha_{\mathrm{app}} = \alpha_\parallel$, when source is located in plane of isotropy

1: Popov & Mandel (1998); for the lower bound, see also (A17)
2: this work; derived from 10.2 (8) and 10.4 (12) of Carslaw & Jaeger (1959)
3: Popov & Mandel (1998); see also Jorand *et al.* (2013)
4: Gustafsson *et al.* (2000)

Table A2. Physical properties of the standard materials used for the Thermal Conductivity Scanning (TCS) at RUB.

Standard material	$\lambda^{\dagger}$ (W m^{-1} K^{-1})	$\alpha^{\dagger}$ 10^{-6} (m^2/s)	c_p ‡ (J kg^{-1} K^{-1})	ρ (kg m^{-3})
glass	0.7	0.4	455	3844±52
fused quartz	1.4	0.9	708	2197±09
marble	3.8	1.5	890	2846±10
titanium alloy	6.1	2.6	531	4421±06
steel	13.3	3.6	467	7904±15

†: thermal conductivity λ and thermal diffusivity α as specified by the manufacturer (Lippmann und Rauen GbR)
‡: isobaric specific heat capacity c_p calculated according to (A8), valid for isotropic materials, using density ρ measured at RUB relying on Archimedes' principle

The spatiotemporal changes of temperature are thus governed by the thermal diffusivity tensor $\boldsymbol{\alpha} = \boldsymbol{\lambda}/(\rho\, c)$ (m^2 s^{-1}), expressing the ratio of transport ability to storage necessity.

For orthorhombic materials, eq. (A4) becomes

$$\lambda_x \frac{\partial^2 T}{\partial x^2} + \lambda_y \frac{\partial^2 T}{\partial y^2} + \lambda_z \frac{\partial^2 T}{\partial z^2} = \rho\, c\, \frac{\partial T}{\partial t} \quad , \tag{A5}$$

when the principal axes of the conductivity tensor coincide with the coordinate axes. Transverse isotropy is a fair approximation for many sedimentary and metamorphic rocks and leads to a thermal conductivity tensor and a thermal diffusivity tensor with two elements each:

$$\boldsymbol{\lambda} = \begin{pmatrix} \lambda_\perp & 0 & 0 \\ 0 & \lambda_\parallel & 0 \\ 0 & 0 & \lambda_\parallel \end{pmatrix} \quad \text{and} \quad \boldsymbol{\alpha} = \begin{pmatrix} \alpha_\perp & 0 & 0 \\ 0 & \alpha_\parallel & 0 \\ 0 & 0 & \alpha_\parallel \end{pmatrix} \quad , \tag{A6}$$

that is, thermal conduction across ($\lambda_x = \lambda_\perp$, $\alpha_\perp = \lambda_\perp/(\rho c)$) and along ($\lambda_y = \lambda_z = \lambda_\parallel$, $\alpha_\parallel = \lambda_\parallel/(\rho c)$) planar structural elements, for example, bedding or foliation. The ordering of diagonal elements in (A6) does not imply their relative magnitude. For isotropic materials with $\lambda_x = \lambda_y = \lambda_z = \lambda$, eq. (A4) simplifies to

$$\alpha \nabla^2 T = \frac{\partial T}{\partial t} \quad , \tag{A7}$$

with the scalar thermal diffusivity

$$\alpha = \frac{\lambda}{\rho\, c} = \frac{\lambda}{\tilde{c}} \quad . \tag{A8}$$

A2 The dependence of thermal conductivity results on measurement direction for transverse isotropy

According to Fourier's law (A2), the thermal conductivity in a direction prescribed by an imposed thermal gradient is

$$\lambda_{\nabla T} = -\frac{q_{\nabla T}}{|\nabla T|} \tag{A9}$$

with the component of the heat flux in the direction of the temperature gradient

$$q_{\nabla T} = \mathbf{q} \cdot \frac{\nabla T}{|\nabla T|} \quad , \tag{A10}$$

where the second factor represents the unit vector of the direction of the thermal gradient. In the principal axes system of the conductivity tensor, the components of the thermal gradient read

$$\nabla T = |\nabla T| \begin{pmatrix} l_1 \\ l_2 \\ l_3 \end{pmatrix}, \tag{A11}$$

where the l_i, $i = 1, 2, 3$ denote the direction cosines, that is, the cosines of the angles between the gradient and the principal axes. Thus, the components of the flux (again in the principal axes system) are

$$\mathbf{q} = -\begin{pmatrix} \lambda_1 & 0 & 0 \\ 0 & \lambda_2 & 0 \\ 0 & 0 & \lambda_3 \end{pmatrix} |\nabla T| \begin{pmatrix} l_1 \\ l_2 \\ l_3 \end{pmatrix} = -|\nabla T| \begin{pmatrix} l_1 \lambda_1 \\ l_2 \lambda_2 \\ l_3 \lambda_3 \end{pmatrix} \quad . \tag{A12}$$

Finally, calculating the dot product in (A10) yields

$$\mathbf{q} \cdot \nabla T = |\nabla T| \begin{pmatrix} l_1 \lambda_1 \\ l_2 \lambda_2 \\ l_3 \lambda_3 \end{pmatrix} \cdot |\nabla T| \begin{pmatrix} l_1 \\ l_2 \\ l_3 \end{pmatrix} = |\nabla T|^2 \left(l_1^2 \lambda_1 + l_2^2 \lambda_2 + l_3^2 \lambda_3 \right) \quad , \tag{A13}$$

and plugging this result into (A9) leads to

$$\lambda_{\nabla T} = \left(l_1^2\lambda_1 + l_2^2\lambda_2 + l_3^2\lambda_3\right) \quad . \tag{A14}$$

The direction cosines obey

$$l_1^2 + l_2^2 + l_3^2 = 1 \quad , \tag{A15}$$

and therefore the isotropic case $\lambda_{\nabla T} = \lambda_1 = \lambda_2 = \lambda_3$ is immediately recovered, that is, the scalar thermal conductivity can be determined by imposing a temperature gradient in any direction. For transversely isotropic media with $\lambda_1 \neq \lambda_2 = \lambda_3$, we find

$$\lambda_{\nabla T}^{\mathrm{ti}} = \lambda_1 l_1^2 + \lambda_2\left(l_2^2 + l_3^2\right) = l_1^2\lambda_1 + \left(1 - l_1^2\right)\lambda_2 = (\lambda_1 - \lambda_2)l_1^2 + \lambda_2 \quad . \tag{A16}$$

If, for a foliated, transversely isotropic material, the principal axis 1 is chosen to coincide with the normal vector to the foliation, the direction cosine l_1 in (A16) corresponds to that of the angle between the direction of the imposed temperature gradient and the normal vector to the foliation plane. Then, for the notation to be illustrative, we denote the two principal components of the thermal conductivity tensor as $\lambda_1 \longrightarrow \lambda_\perp$ and $\lambda_2 = \lambda_3 \longrightarrow \lambda_\parallel$, characterizing heat flow perpendicular to and in the foliation planes, respectively. Furthermore, the core geometry of the tested samples suggests to use dip γ and strike θ of the foliation for classification of a specific experimental constellation. The angle between the normal vector to the foliation and the direction of the thermal gradient is identical to the dip angle γ, for measurements in axial direction, and thus (A16) gives

$$\lambda_{\mathrm{axial}}^{\mathrm{ti}}(\gamma) = \lambda_\perp \cos^2(\gamma) + \lambda_\parallel \sin^2(\gamma) = \left(\lambda_\perp - \lambda_\parallel\right)\cos^2\gamma + \lambda_\parallel \quad . \tag{A17}$$

Eq. (A17) applies to the experimental configuration of the steady-state divided bar measurements, but for effects due to the finite size of samples. Evaluation of such an axial measurement thus provides an apparent thermal conductivity, which is a convolution of the two true thermal conductivity tensor elements and the actual orientation of the sample. Likewise, analytical relations for such apparent thermal conductivities of anisotropic media are known for several transient methods yield (Table 2). Scan lines perpendicular and parallel to the planes of isotropy yield non-intuitive apparent conductivities of $\lambda_\parallel$ and $\sqrt{\lambda_\perp\lambda_\parallel}$, respectively. The average of the apparent conductivity results of two radial scan lines normal to each other is insensitive to their actual orientation relative to the strike of the planes of isotropy; the apparent conductivity gained from averaging is closely approximated by the identical ones from scan lines parallel and perpendicular to the strike. The modified Ångström method gives a principle thermal diffusivity (or conductivity in case specific heat capacity is independently known), when the line, on which the two thermocouples are placed, coincides with the corresponding principal axis. The transient plane source approach gives the full set of thermal parameters of a transversely isotropic medium, when the source is placed in the plane of isotropy and the specific heat capacity is independently determined.

APPENDIX B: EMPLOYED METHODS FOR DETERMINING THERMAL PROPERTIES

We employed six methods in total that differ in their geometrical specifics and in investigated sample size (Table 2).

B1 Dewar flask method (RUB)

Specific heat capacity was derived from water–temperature measurements conducted in an insulated Dewar flask (KGW Isotherm Karlsruher Glastechnisches Werk–Schieder GmbH). The samples prepared for the measurements at RUB with the modified Ångström device (Table C1) were heated to $T_{0,s} \sim 60\,^{\circ}\mathrm{C}$ and then submersed in deionized water (initial temperature $T_{0,w}$) filling the flask, which was instantly sealed with its insulating cap. Water temperature was continuously recorded until a constant temperature T_{end} was reached indicating thermal equilibration between the water and the rock sample. Isobaric specific heat capacity was calculated using

$$c_p = \frac{m_w c_{p,w} + C_{Dewar}}{m_s} \frac{T_{end} - T_{0,w}}{T_{0,s} - T_{end}} \quad , \tag{B1}$$

where m_s denotes mass of the sample (kg), m_w mass of the deionized water (kg) and $c_{p,w}$ the isobaric specific heat capacity of water ($\mathrm{J\,kg^{-1}\,K^{-1}}$). The heat capacity ($C_{Dewar}$) of the flask was determined to be 129($\pm$30) $\mathrm{J\,K^{-1}}$ by measuring equilibrium temperatures of water mixtures of different starting temperatures. A neglect of the heat-uptake of the Dewar flask leads to an underestimation of specific heat capacity up to about 100 $\mathrm{J\,kg^{-1}\,K^{-1}}$. The analysis based on (B1) neglects the temperature dependence of specific heat capacity of either rock sample or water. In the relevant temperature range, either is $\sim 1\,\mathrm{J\,kg^{-1}\,K^{-2}}$ according to amount, but positive for rocks and negative for water, and thus their effects are partly counterbalancing each other and give rise to an underestimation of the specific heat capacity on the order of only 10 $\mathrm{J\,kg^{-1}\,K^{-1}}$.

Individual c_p measurements lasted up to 40 min and were repeated three times yielding an average standard deviation of about 5 per cent. Relative uncertainties in the c_p values were determined by Gaussian error propagation and ranged from 8 to 13 per cent, with an average of $\sim$10 per cent. The heat capacity values determined by the Dewar flask method for the standards used for the TC scanner closely agree with the values calculated according to (A8) from λ and α quoted by the manufacturer of the TC scanner and density determined at RUB (Fig. 4).

B2 Divided bar apparatus (UCD)

The divided bar method is a comparative method deriving thermal conductivity from a temperature drop over a sample and two standards in a steady-state regime employing Fourier's law (A2). Divided bar experiments were conducted at UCD using a device constructed following the design of Sibbitt *et al.* (1978) and tested by McGuinness *et al.* (2014), who quote a repeatability of 7 per cent or better.

B3 Transient divided-bar apparatus (AU)

Bording *et al.* (2016) extended the classical divided bar technique to transient measurements that allow for determining the full set of thermal properties. Generally, three individual, independent measurements were performed on each sample. During a measurement, a number of heat pulses are generated by the heat source. Temperature-time series are recorded and processed by solving the 1D heat equation along the axis of the divided bar apparatus using finite differences and by employing a Markov Chain Monte Carlo Metropolis Hastings inversion algorithm, which tests combinations of λ and $\tilde{c}$ (five times, 50 000 iterations) to achieve a match of numerical and experimental temperature transients. The numerical solution accounts for thermal resistance between the stacked discs. Thermal diffusivity α is calculated from each inverted parameter pair after (A8). Each inversion run provides mean values and standard deviations of the sample's thermal properties. Mean and standard deviation are calculated for the five inversion results from each measurement and then for the results from the three individual measurements providing the reported mean values with standard deviations, by which 1 to 3 per cent precision and repeatability are reflected. Accuracy depends on the accuracy of the applied standard reference material and is within the range of 5 to 10 per cent (Bording *et al.* 2016), with a better accuracy for thermal conductivity than for thermal diffusivity.

B4 Transient plane source (CU)

Experiments at CU were conducted with a Hot Disk® Thermal Constant Analyser TPS 2500 S to determine λ and α. This transient plane-source device uses a metal spiral (hot disc), which simultaneously acts as heat source and temperature sensor. During an experiment, voltage and resistance are recorded as a function of time. Resistivity changes are determined to infer changes of the spiral temperature, directly linked to the sample's thermal transport properties (Gustafsson 1991; He 2005). Gustafsson (1991) originally reported uncertainties of 3 per cent for λ and 7 per cent for α. According to ISO-22007-2, the accuracy for thermal conductivity is estimated at 2 per cent to 5 per cent and for the diffusivity at 5 per cent to 10 per cent in routine measurements at or around room temperature. An extensive theoretical account of the method's accuracy is presented by Zhang *et al.* (2017).

B5 Optical scanning (SGU, RUB)

The two identical TC scanners, designed by Lippmann und Rauen GbR and operated at SGU and RUB, are based on the work of Popov *et al.* (1985). They allow for determination of λ and α along a surface profile of a flat or cylindrical (rock) sample. Three temperature sensors and

an infrared heat source (HS) are moved at constant velocity beneath the sample that is placed between two standards with known thermal properties (Fig. A3, Table A2).

Temperatures are recorded every mm of travel of the measurement table. For each measurement spot, thermal conductivity and diffusivity are automatically calculated from the relations given by Popov *et al.* (1985). The manufacturer provides uncertainty values of 3 per cent for λ and 5 per cent for α over a measurement range from 0.2 to 25 $W\,m^{-1}\,K^{-1}$ for λ and 0.6×10^{-6} to 3×10^{-6} $m^2\,s^{-1}$ for α, respectively (TCS Manual, 2015). Specific heat capacity is calculated according to (A8) assuming isotropy complementing TC scan results for λ and α with independently measured density ρ. Gaussian error propagation for the calculation of c_p leads to an uncertainty of 6 per cent.

B6 Modified Ångström device (RUB)

A modified Ångström device (Andolfsson 2019) was used at RUB to determine thermal diffusivity based on analysing changes in phase and amplitude of harmonic temperature signals at two positions in a sample experiencing periodic heating (Ångström 1862). A 3 mm wide copper spiral acts as a pseudo-point source emitting pulsed heat signals into the samples above and below (Fig. A4); temperature is measured using two K-type thermocouples placed in two holes with a diameter of ∼2 mm drilled perpendicular to the cylindrical axis, to the centre of the samples at distances of $a = 5$ and $b = 10$ mm from the source. The stack of samples and heater is axially loaded with 0.1 kN, that is, 0.14 MPa for the used samples with a diameter of 30 mm, to ensure thermal contact between the heater and the samples. Energy input is computer-controlled, and temperatures are recorded digitally.

The recorded data set comprises two temperature-time readings, one for each thermocouple. The transient associated with continuous heating superimposed to the oscillatory variation is subtracted from each reading (detrending). Subsequently, amplitude ratio δ and phase shift φ of the two signals are determined for the imposed period using fast Fourier transformation. To constrain the uncertainties of amplitude ratio and phase shift, we performed a sliding window analysis, in which δ and φ are determined for a window with a length of four periods, which was successively shifted over the entire signal length in steps of ∼1 per cent of a period.

Analysis of the experimental data is based on the analytical solution of the diffusion equation for a point source assuming a homogeneous and isotropic medium, according to which thermal diffusivity relates to amplitude ratio (dimensionless) by

$$\alpha_\delta = \frac{\omega}{2}\left[\frac{b-a}{\ln\left(\frac{b}{a}\delta\right)}\right]^2 \tag{B2}$$

and to phase shift (in radians) by

$$\alpha_\varphi = \frac{\omega}{2}\left[\frac{b-a}{\varphi}\right]^2 \quad , \tag{B3}$$

where a and b represent the distances (m) from the source to the two thermocouples (Fig. A4) and ω (s^{-1}) denotes angular frequency. Combining (B2) and (B3) yields

$$\delta = \frac{a}{b}e^{-\varphi} \quad . \tag{B4}$$

Typically, a pair of mean δ and φ values does not plot exactly on the ideal point source relation (B4). Thus, (B2) and (B3) cannot be directly used to calculate α. Instead, the uncertainties in δ and φ are used to enclose the range of δ and φ values honouring the theoretical relation (B4). This approach provides a range of 'equivalent' thermal diffusivity values of a hypothetical homogeneous and isotropic medium consistent with the experimental data (Fig. A4). We use the standard deviation gained from parameters for all sliding windows to derive an ellipse representing the expected variability from the mean for δ and φ. Subsequently, the mid-point of the line described by (18) within the ellipse is determined and used to calculate α (Fig. A4). Numerical modelling (Andolfsson 2019) suggests that neither finite source size, including subordinate effects of lateral heat losses, nor misplacement of source and disturbance of the temperature field by the thermocouples significantly affect the results.

Thermal conductivity is calculated from (A8), assuming isotropy, by combining the determined thermal diffusivity value with specific heat capacity constrained by the Dewar measurements and density determinations. Gaussian error propagation accounting for the determined errors in α, c_p and ρ yields uncertainties in thermal conductivity from ±12 to ±15 per cent with an average around ±13 per cent.

APPENDIX C: DIMENSIONS OF PREPARED SAMPLES

Table C1. Dimensions of samples investigated in the various research laboratories.

Research organization	Method	Diameter (mm)	Height (mm)
Chalmers University (CU)	Plane source	40–50	20–25
Geological Survey of Sweden (SGU)	Optical scanning	40	20
Ruhr-Universität Bochum (RUB)	Dewar method	30	50
	Modified Ångström	30	50
	Optical scanning	35–61	50–60
Aarhus University (AU)	Transient divided bar	35–50	15–20
University College Dublin (UCD)	Steady-state divided bar	35–48	18–22

Table C2. Density of COSC-1 cores, the cylindrical samples prepared from them and reference materials, as determined at RUB und UCD.

ID[1] or material type	Density (kg m^{-3})		
	cores	samples(RUB)	samples(UCD)
C7Z1	2720±4	2722±4	2707
C150S2	2967±4	2969±4	2968
C272S1	2676±4	2678±4	2692
C309S3	2613±4	2615±4	2324
C404S2	2695±4	2697±4	2709
C470S4	3001±4	3003±4	3006
C635S5	2676±4	2679±4	2687
C652S1	2682±4	2685±4	2699
C686S1	2689±4	2692±4	2698
Carrara marble	–	2699±4	2785
Westerly granite (orange)	–	2628±4	2644
Pyrophyllite	–	2724±4	2723
Al_2O_3 ceramic (Degussit AL23)	–	3915±4	3930

1: see Table 4 for IGSN

The requirements regarding sample geometry substantially vary between the methods (Table C1).

APPENDIX D: DENSITY MEASURED BY UCD AND RUB FOR ALL COSC-1 SAMPLES AND REFERENCE MATERIALS

The results of the density measurements in two laboratories correlate well but for a single outlier, likely related to sample-to-sample variability

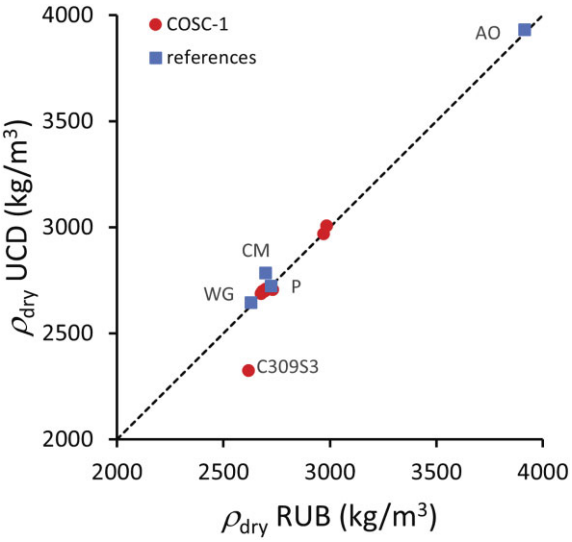

Figure D1. Density (ρ) measurements by UCD and RUB for all COSC-1 samples (circles) and reference samples (squares, CM: Carrara marble; WG: Westerly granite; P: pyrophyllite; AO: aluminium oxide). The symbol size exceeds the size of the error bars. The outlier among the COSC-1 cores, C309S3, is a pegmatite.

(Fig. D1).

APPENDIX E: MINERAL PHASES AND AVERAGE VOLUME FRACTIONS OF COSC-1 SAMPLES

Mineral phases were identified by thin-section analyses and their average volume fractions and standard deviations were estimated relying on point counting (Table E1).

Table E1. Mineral phases and their average volume fractions and standard deviations determined from point counting on thin sections; the standard deviations reflect the variability on four counting lines. The fraction of the dominant mineral in a sample is presented by bold font, and values in italic font give the minerals with a fraction below 10 per cent.

Mineral	C7Z1	C150S2	C272S1	C309S3	C404S2	C470S4	C635S5	C652S1	C686S1
Quartz	**0.43**±0.06	0.23±0.03	**0.67**±0.06	**0.38**±0.05	**0.41**±0.05	0.10±0.03	**0.80**±0.01	**0.73**±0.03	**0.80**±0.01
Carbonate	0.16±0.01	–	0.11±0.01	–	0.17±0.05	*0.01*±0.01	*0.03*±0.01	*0.02*±0.04	*0.01*±0.06
Biotite	–	0.15±0.05	0.18±0.02	*0.02*±0.01	*0.03*±0.01	–	*0.06*±0.01	0.10±0.02	*0.01*±0.03
Muscovite	–	–	–	*0.01*±0.01	–	–	*0.09*±0.00	0.12±0.01	0.12±0.00
Chlorite	–	–	–	–	–	–	*0.01*±0.00	*0.03*±0.00	*0.05*±0.01
Garnet	–	–	–	–	–	–	*0.01*±0.00	*0.00*±0.00	–
Plagioclase	*0.09*±0.03	0.14±0.03	*0.03*±0.02	0.12±0.06	*0.09*±0.04	*0.08*±0.05	*0.01*±0.00	–	*0.01*±0.00
Microcline	0.15±0.03	–	–	**0.47**±0.11	0.16±0.04	0.17±0.08	–	–	–
Amphibole (Hbl)	0.18±0.02	**0.49**±0.04	*0.02*±0.01		0.13±0.02	**0.63**±0.04	–	–	–

APPENDIX F: LITERATURE VALUES USED FOR MIXING-MODEL CALCULATIONS

A comprehensive compilation of mineral thermal properties, not cited in Table F1, can be found in Cermak & Rybach (1982).

Table F1. Values of thermal capacity $\tilde{c}$ and thermal conductivity λ used for mixing-model calculations. If reported, minimum and maximum components of the thermal conductivity tensor are given along with the corresponding crystallographic axis/plane (lower case).

Mineral	Thermal capacity ($MJ\ m^{-3}\ K^{-1}$)	Thermal conductivity	($W\ m^{-1}\ K^{-1}$)	Reference[1]
Quartz	2.0	λ_{VRH}	7.7	Horai (1971)
	–	λ_a	6.2	Birch & Clark (1940)
	–	λ_c	10.3	Birch & Clark (1940)
Calcite	2.4[2]	λ_{VRH}	3.6	Horai (1971)
	–	λ_a	3.2	Birch *et al.* (1942)
	–	λ_c	3.7	Birch *et al.* (1942)
Biotite	2.3	λ_{VRH}	2.0	Horai & Simmons (1969)
	–	$\lambda_{[001]}$	0.5	Diment & Pratt (1988)
	–	$\lambda_{[100]/[010]}$	3.1	Diment & Pratt (1988)
Muscovite	2.2	λ_{VRH}	2.3	Horai & Simmons (1969)
	–	$\lambda_{[001]}$	0.6	Diment & Pratt (1988)
	–	$\lambda_{[100]/[010]}$	3.9	Diment & Pratt (1988)
Chlorite	1.7	λ_{VRH}	3.0	Clauser & Huenges (1995)
Garnet	2.5[3]	λ_{VRH}	3.6	Horai & Simmons (1969)
Plagioclase	1.9[4]	λ_{VRH}	2.1[5]	Horai & Simmons (1969)
Microcline	1.8	λ_{VRH}	2.4	Horai & Simmons (1969)
Amphibole (Hbl)	2.4	λ_{VRH}	2.5	Horai & Simmons (1969)

1: references refer to thermal conductivity values; all thermal capacity values are taken from the compilation of Waples & Waples (2004)
2, 3, and 4: arithmetic means of calcite and dolomite, almandine and grossularite, and albite and anorthite, respectively
5: arithmetic mean of albite and oligoclase

APPENDIX G: COMPARISON OF THERMAL SCANNING OF CORES AND SAMPLES AT RUB

Thermal conductivity and thermal diffusivity results from optical scanning at RUB on cores before preparation and samples prepared for the interlaboratory comparison very closely agree (Fig. G1) but for the thermal conductivity of the coarse-grained Paragneiss (C7Z1) and the Amphibolite (C470S4). The rocks with the largest fraction of anisotropic minerals yielded the largest conductivity and diffusivity values.

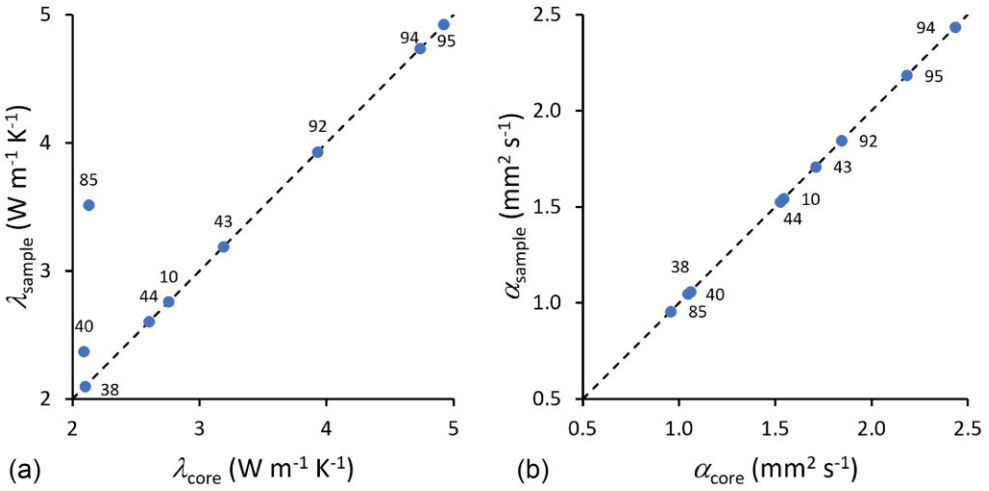

Figure G1. Correlation of (a) thermal conductivity and (b) thermal diffusivity determined by optical scanning at RUB on COSC-1 cores before preparation and on samples prepared for the interlaboratory comparison. The data points are labelled by the fraction of anisotropic minerals.

APPENDIX H: SUPPLEMENTARY MEASUREMENTS

Six further cores from COSC-1 (Table H1) were optically scanned every 45° on the cylinder walls and on the two end faces by the RUB team (Fig. H1) to eliminate the effect of sample-to-sample and instrument variability affecting the interlaboratory comparison.

Table H1. COSC-1 core pieces selected for detailed TC scanning at RUB.

IGSN[1] ICDP5054...	C#S#[2]	Depth[3] (m)	Diameter (mm)	Lithology	Dip[4] (°)
EX52601	C432S4	1336.7	~ 61	amphilbolitic gneiss	~ 30°
EXE2601	C513S1	1568.1	~ 61	amphilbolitic gneiss	~ 0°
EXG2601	C528S4	1613.3	~ 61	Calc-silicate gneiss	~ 10°
EXF6601	C689S1	2448.3	~ 47	paragneiss	~ 10°
EXH6601	C694S5	2482.3	~ 47	mylonite	~ 10°
EXI6601	C696S7	2495.6	~ 47	mylonite	~ 10°

1: International GeoSample Number (drill hole ICDP 5054-1-A); access at, for example, https://dataservices.gfz-potsdam.de/igsn/icdp/index.php?igsn=ICDP5054EX52601
2: Core number and section number
3: Driller's depth
4: Dip of foliation relative to the core cylinder top determined with protractor.

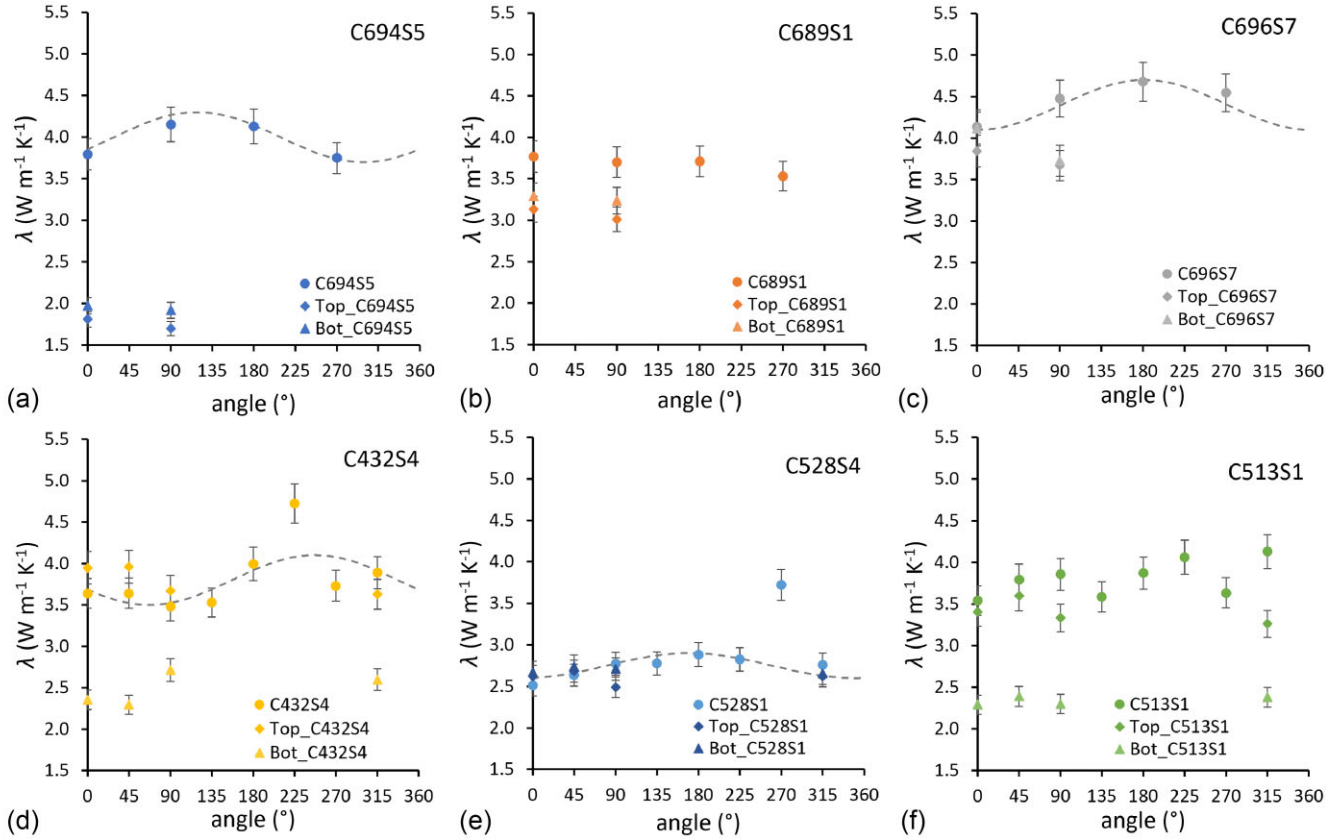

Figure H1. (a) to (f) Results of axial and radial scans on further COSC-1 cores, performed at RUB. Results of the radial scans on the end faces (diamonds: top, triangles: bottom) tend to give lower conductivities than the axial measurements (circles), representing an anisotropy opposite to the sample suite of the interlaboratory study. In two cases (a, b), the radial measurements on the two end faces significantly differ. The axial measurements show scatter that barely exceeds the experimental uncertainty but for a few prominent outliers, for example, in (c). Nevertheless, a systematic 'harmonic' variation with measurement angle appears possible for several samples, as tentatively indicated by the dashed lines. If real, such a variation would be at odds with the predictions gained from assuming transverse isotropy (see Table A1).